Key Points:
- Seismicity is sparse near the Alpine Fault late in its typical seismic cycle
- Seismicity rates increase abruptly 9 km southeast of the fault trace
- This transition coincides with a strain rate peak and lateral velocity gradients

Supporting Information:
- Supporting Information S1
- Data Set S1

Correspondence to:
S. Bourguignon,
s.bourguignon@gns.cri.nz

Structural heterogeneity of the midcrust adjacent to the central Alpine Fault, New Zealand: Inferences from seismic tomography and seismicity between Harihari and Ross

Sandra Bourguignon[1], Stephen Bannister[1], C. Mark Henderson[1], John Townend[2], and Haijiang Zhang[3]

[1]GNS Science, Lower Hutt, New Zealand, [2]School of Geography, Environment and Earth Sciences, Victoria University of Wellington, Wellington, New Zealand, [3]Laboratory of Seismology and Physics of Earth's Interior, School of Earth and Space Sciences, University of Science and Technology of China, Hefei, China

Abstract Determining the rates and distributions of microseismicity near major faults at different points in the seismic cycle is a crucial step toward understanding plate boundary seismogenesis. We analyze data from temporary seismic arrays spanning the central section of the Alpine Fault, New Zealand, using double-difference seismic tomography. This portion of the fault last ruptured in a large earthquake in 1717 AD and is now late in its typical 330 year cycle of Mw$\sim$8 earthquakes. Seismicity varies systematically with distance from the Alpine Fault: (1) directly beneath the fault trace, earthquakes are sparse and largely confined to the footwall at depths of 4–11 km; (2) at distances of 0–9 km southeast of the trace, seismicity is similarly sparse and shallower than 8 km; (3) at distances of 9–20 km southeast of the fault trace, earthquakes are much more prevalent and shallower than 7 km. Hypocenter lineations here are subparallel to faults mapped near the Main Divide of the Southern Alps, confirming that those faults are active. The region of enhanced seismicity is associated with the highest topography and a high-velocity tongue doming at 3–5 km depth. The low-seismicity zone adjacent to the Alpine Fault trace is associated with Vp and Vs values at midcrustal depths about 8 and 6% lower than further southeast. We interpret lateral variations in seismicity rate to reflect patterns of horizontal strain rate superimposed on heterogeneous crustal structure, and the variations in seismicity cutoff depth to be controlled by temperature and permeability structure variations.

1. Introduction

The 300–500 km long central portion of the Alpine Fault, New Zealand (Figure 1) last ruptured in a large earthquake (Mw$\sim$8) in approximately 1717 AD [*Sutherland et al.*, 2006, 2007]. Ruptures of the southern section of the Alpine Fault ($>$150 km south of this study) have a return period of about 329 ± 68 years [*Berryman et al.*, 2012], suggesting that the fault may be reaching the end of the typical interseismic period.

Here we derive microearthquake locations and crustal seismic properties (Vp, Vs, and the Vp/Vs ratio) in the central section of the Alpine Fault between Harihari and Ross. This segment of the Alpine Fault is located about 25 km north of the township of Whataroa and the site of the Deep Fault Drilling Project (DFDP) [*Townend et al.*, 2009], a scientific drilling project addressing the structure and ambient conditions of the central Alpine Fault [*Sutherland et al.*, 2012; *Townend et al.*, 2013]. The Harihari to Ross segment of the Alpine Fault is noteworthy on account of the higher level of seismicity compared to the region immediately southwest (Figure 1) [*Anderson and Webb*, 1994; *Boese et al.*, 2012; *Eberhart-Phillips*, 1995; *Leitner et al.*, 2001], permitting a detailed comparison of the locations of microearthquakes with tomographic images of crustal structure. The seismicity and tomographic results provide insight into the rheology of the plate boundary zone and, in particular, factors controlling the depth and geometry of the seismic-aseismic transition late in the average long-term seismic cycle of the Alpine Fault.

1.1. Tectonic Setting and Previous Studies

The Alpine Fault is a $\sim$600 km long continental transform linking two subduction zones of opposite polarity in the north and south of the South Island. The central portion of the fault strikes at 055°, 10–15° counterclockwise of the present-day Australia-Pacific relative plate motion direction [*Beavan et al.*, 2002; *Cande and*
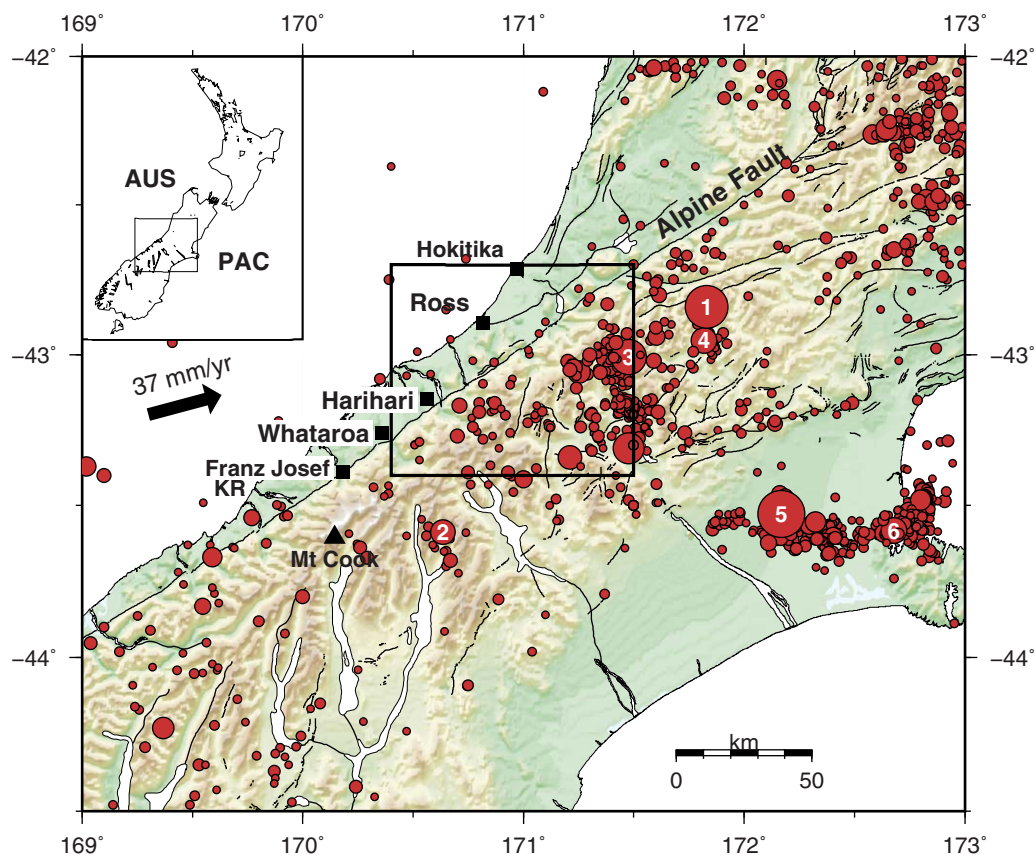
Figure 1. Map of the central South Island showing the position of the Alpine Fault, magnitude 4+ earthquakes recorded since 1900 (http://www.geonet.org.nz) and topographic relief. The square delimits the region of this study (Figure 2). Mount Cook is shown as a triangle. Small squares indicate townships. Abbreviation KR indicates the location of the Karangarua River mouth. The thick black arrow denotes the Australia-Pacific relative plate motion [*DeMets et al.*, 1994]. AUS and PAC denote the Australian and Pacific plates. Numbered red circles indicate historical earthquakes: (1) the 1929 M_W 7.0 Arthur's Pass earthquake, (2) the 1984 M_W 6.1 Godley earthquake, (3) the 1994 M_W 6.7 Arthur's Pass earthquake, (4) the 1995 M_W 6.2 Cass earthquake, (5) the 2010 September M_W 7.2 Darfield earthquake, and (6) the 2011 February M_W 6.2 Christchurch earthquake. The top left insert shows New Zealand and this map location.

Stock, 2004; *DeMets et al.*, 1994] and at approximately 60° to the regional axis of maximum horizontal compressive stress [*Boese et al.*, 2012; *Townend et al.*, 2012]. Deformation along the central Alpine Fault is therefore transpressive, with components of interplate motion of 35–39 mm/yr parallel and 6–10 mm/yr perpendicular to the Alpine Fault [*Beavan et al.*, 2002; *Cande and Stock*, 2004; *DeMets et al.*, 1994; *Norris and Cooper*, 2007; *Walcott*, 1998].

Dextral movement on the Alpine Fault has offset terranes on either the side of the fault by 440–470 km [e.g., *Sutherland*, 1999], juxtaposing Paleozoic-Mesozoic rocks originating from the break-up of Gondwana in the west with schistose metasedimentary terranes formed by accretion onto the Gondwana margin in the east [*Mortimer*, 2004].

The Alpine Fault has a highly linear trace overall, but 50–150 km southeast of this study area the fault is serially partitioned at shallow depths and on length scales of 1–10 km into easterly strike-slip segments connected by more northerly-striking oblique thrust segments [*Norris and Cooper*, 1997, 2007]. At shallow depth (<600 m) and on length scales of 1–1000 m, the fault is parallel-partitioned into asymmetric 200–600 m wide flower structures in the hanging wall, bounded by dextral-normal and dextral-thrust faults rooting into a planar, moderately southeast-dipping, dextral-reverse fault plane [*Barth et al.*, 2012]. In the present study area, by contrast, the fault trace is essentially straight but thrusts have locally developed in the footwall [*Norris and Cooper*, 2007]. Further north, the Alpine Fault changes character again as slip is progressively distributed onto ENE-striking faults comprising the Marlborough fault system and correspondingly lower amounts of slip are accommodated on the Alpine Fault [*Langridge et al.*, 2010].

Paleoseismic data yield Late Quaternary strike-slip and dip-slip rates of 27 ± 5 and 6–12 mm/yr, respectively, on the central Alpine Fault, accounting for 70–75% of the fault-parallel interplate motion and a variable proportion of ~70% of the fault-perpendicular motion [*Norris and Cooper*, 2001]. Shear strain rates indicate that the bulk of the remainder, about 10 mm/yr, is accommodated southeast of the Alpine Fault [*Beavan et al.*, 2007] on faults distributed through the Southern Alps and in the eastern foothills [*Beavan et al.*, 2010; *Cox et al.*, 2012; *Wallace et al.*, 2006]. Historical earthquakes, such as the 1994 M_W 6.7 Arthur's Pass earthquake and aftershocks [*Bannister et al.*, 2006] (Figure 1), represent present-day coseismic strain release 25–40 km southeast of the Alpine Fault.

The Alpine Fault has been interpreted to form a southeast-dipping ramp along which the Alpine Schist is uplifted [e.g., *Grapes*, 1995; *Little et al.*, 2002]. The hanging wall assemblage is of amphibolite facies near the fault and of prehnite-pumpellyite facies further than ~20 km southeast of the surface trace of the Alpine Fault to near the Main Divide [e.g., *Cox and Sutherland*, 2007]. The seismic anisotropy of the Alpine Schist increases with metamorphic grade toward the fault [*Okaya et al.*, 1995]. Maximum *P* and *S* wave anisotropy of 20 and 26% have been measured on samples of schist of the highest metamorphic grade [*Christensen and Okaya*, 2007]. A 1–2 km thick layer of basal mylonites separates the schists from the Alpine Fault damage zone [*Reed*, 1964; *Sibson et al.*, 1979]. The mylonites are inferred to have formed at depths of 20–30 km under amphibolite facies conditions [*Grapes and Watanabe*, 1992; *Grapes et al.*, 1994; *Holm et al.*, 1989].

1.2. Alpine Fault Geometry and Seismological Characteristics

Exposed gouge zones and mylonitic foliations imply that the central Alpine Fault dips at 30–60°SE in the midcrust [*Cooper and Norris*, 1994; *Little et al.*, 2002; *Norris and Cooper*, 2007]. At Harold Creek near Harihari (Figure 1), mylonite foliations dip $47 \pm 11°$ (1σ) to the southeast [*Little et al.*, 2013]. Information on the deeper Alpine Fault structure and deformation processes occurring within the Southern Alps crustal root is provided by two geophysical northwest-southeast transects, SIGHT T1 and T2, collected in 1996 and 1998 across the South Island [*Okaya et al.*, 2007]. The northern transect T1 passed through the Whataroa River Valley about 25 km southwest of this study. The southern transect T2 ran about 80 km southwest of this study, south of the township of Fox Glacier.

Seismic data collected along SIGHT transect T1 [*Okaya et al.*, 2007] along the Whataroa Valley reveal a weak reflector at about 1 s two-way time (~2 km depth) with an apparent dip of ~25° to the southeast, which would project to the surface west of the Alpine Fault trace, but no clear reflection of the Alpine Fault thrust [*Davey*, 2010]. *Davey* [2010] interpreted the reflector as either a fault lying in the Alpine Fault footwall or as an abandoned section of the Alpine Fault thrust dipping obliquely to the seismic profile.

Along SIGHT transect T2 [*Scherwath et al.*, 2003], seismic data reveal a zone of high reflectivity dipping 60°SE at 15 km depth and flattening to a near-horizontal dip at ~30 km depth [*Stern et al.*, 2007]. *Stern et al.* [2007] proposed that the strong reflectivity is produced by pockets of fluid released by metamorphic dehydration along the Alpine Fault. At similar depths, seismic tomography reveals a region of high *P* wave attenuation (Qp < 100) dipping to the southeast and interpreted to represent the presence of fluids in the lower crust associated with the downdip extension of the Alpine Fault [*Eberhart-Phillips et al.*, 2008].

Further north, along SIGHT transect T1 [*Van Avendonk et al.*, 2004], the presence of fluids is also supported by magnetotelluric data which reveal a near-vertical low-resistivity region at 5–10 km depth dipping 50–60°SE within the 15–30 km depth range that is indicative of interconnected metamorphic fluids in the mid to lower crust [*Wannamaker et al.*, 2002]. The 20–30 km deep low-frequency earthquakes [*Chamberlain et al.*, 2014] and >30 km deep seismic tremor [*Wech et al.*, 2012, 2013] occurring about 100 km south of this study appear to be associated with the high-attenuation zone and, hence, the zone of enhanced pore fluid pressure [*Wech et al.*, 2012]. Low-effective stresses resulting from high fluid pressures have been hypothesized to facilitate tremor activity [*Audet et al.*, 2009; *Wech et al.*, 2012].

Along and above the 30 km deep zone of reflectivity, modeling of wide-angle *P* wave travel times along SIGHT transect T2 [*Scherwath et al.*, 2003; *Stern et al.*, 2001] reveals a 6–10% reduction of *P* wave speeds also consistent with the presence of high fluid pressure in the crustal root [*Stern et al.*, 2001]. A similar wave speed reduction was imaged along SIGHT transect T1 [*Van Avendonk et al.*, 2004] closer to our study area. Recent analysis shows that metamorphic dehydration during rapid, near-isothermal exhumation of the

Alpine Schists is likely to be the largest contribution to the fluids in the midcrust rather than prograde metamorphism [*Vry et al.*, 2010].

Previous microseismicity studies [*Boese et al.*, 2012; *Eberhart-Phillips*, 1995; *Leitner et al.*, 2001; *O'Keefe*, 2008; *Reyners*, 1988] focused on the region 40–100 km southwest of the present study area have demonstrated that rates of present-day seismicity decrease with proximity to the Alpine Fault and that a triangular region ∼30 km south of this study is nearly aseismic. These studies revealed maximum seismogenic cutoff depths of ∼8 km [*Leitner et al.*, 2001] and 8 ± 2 km [*Boese et al.*, 2012] within 20 km southeast of the Alpine Fault, increasing to 15 ± 2 km further to the southeast [*Boese et al.*, 2012]. Dislocation modeling of vertical velocities [*Beavan et al.*, 2010] across the central Alpine Fault indicates that coupling on the Alpine Fault diminishes below 7–13 km depth and falls to zero in the 13–18 km depth range. Observations of seismic tremor [*Wech et al.*, 2012, 2013] and low-frequency earthquakes [*Chamberlain et al.*, 2014] approximately 100 km south of this study area suggest that there the transition from stick slip to stable sliding on the fault occurs below 25 km depth.

There is a large gradient in horizontal and vertical velocities within 10 km southeast of the Alpine Fault [*Beavan et al.*, 1999, 2010; *Lamb and Smith*, 2013]. Computed shear strain rates [*Beavan and Haines*, 2001] reach a maximum of 5×10^{-7} year^{-1} within a ∼20 km wide zone adjacent to the Alpine Fault. Strain rates of the order of 10^{-12} to 10^{-11} s^{-1} (∼8×10^{-5} year^{-1}) [*Norris and Cooper*, 2003; *Toy et al.*, 2013] have been inferred from Alpine Fault mylonites that form at 20–30 km depth, indicating locally very high strain rates at those depths. Numerical models developed to interpret the GPS velocities also suggest strain rates of 10^{-12} s^{-1} localized along the Alpine Fault ductile shear zone downdip of the locked portion of the fault, i.e., from 5 to 10 km distance southeast of the fault trace [*Ellis et al.*, 2006].

1.3. Vertical Uplift and Thermal Structure

Maximum uplift rates of 4–10 mm/yr [*Beavan et al.*, 2007, 2010; *Wellman*, 1979] are measured near Franz Josef and Fox Glaciers, 50–70 km south of this study area. The faster uplift rates in that region are thought to be promoted by steepening of the Alpine Fault's dip from ∼30 to ∼60° [*Little et al.*, 2005]. At that location, the Southern Alps are interpreted to have reached a steady state [*Adams*, 1981; *Allis and Shi*, 1995; *Batt and Braun*, 1999; *Koons*, 1989, 1995] in which erosional flux, topography, thermal structure, and exhumation are stationary [e.g., *Willett and Brandon*, 2002].

Recent temperature measurements in the DFDP-1B borehole at Gaunt Creek, near Whataroa, yield a hanging wall geothermal gradient of 62.6 ± 2.1°C/km [*Sutherland et al.*, 2012], substantially higher than the nearest estimate of the footwall geotherm of 37 ± 8°C/km [*Townend*, 1999]. The DFDP-1B measurements reinforce the hypothesis that uplift and exhumation east the Alpine Fault have raised isotherms, weakening the crust and focusing deformation along the fault [*Koons*, 1987].

A high geothermal gradient is also implied by young fission tracks and other thermochronological ages [*Adams*, 1981; *Batt and Braun*, 1999; *Chamberlain et al.*, 1995; *Hawkes*, 1991; *Little et al.*, 2005; *Tippett and Kamp*, 1993] and by fluid inclusion analyses, which indicate temperatures of 300–350°C at 5–8 km depth assuming a hydrostatic fluid pressure regime [*Craw*, 1997; *Jenkin et al.*, 1994; *Toy et al.*, 2010]. Thermometry of veins and biotite minerals from Alpine Fault mylonites [*Toy et al.*, 2010] indicates that the geothermal gradient in Alpine Fault mylonites is similar to that in the immediately adjacent hanging wall Alpine Schist, suggesting that isotherms may be flatter than suggested by previous thermal modeling [*Koons*, 1987; *Shi et al.*, 1996]. The high geothermal gradient resulting from uplift and erosion of the Southern Alps is likely the key reason why the brittle-ductile transition and the locking depth of the Alpine Fault are observed to be relatively shallow [*Boese et al.*, 2012].

2. Analysis

2.1. Seismicity Data Set

We analyze continuous seismic waveform data recorded with two temporary seismic arrays, ALFA08 and ALFA09, which were deployed consecutively between Harihari and inland-Hokitika (Figure 2) between 2008 and 2010. The ALFA08 array consisted of eight sensors spaced 10–50 km apart and operated from October 2008 to October 2009 (blue triangles in Figure 2). The second deployment, ALFA09 (red triangles in Figure 2)
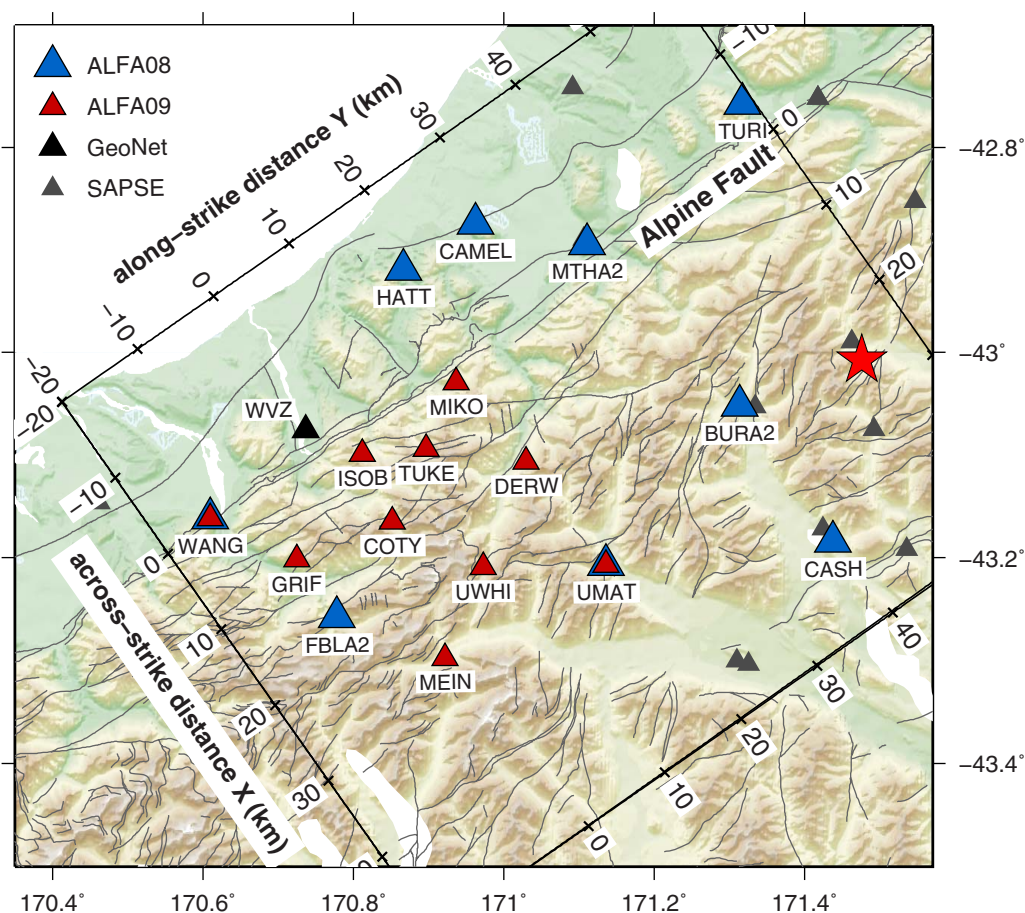
Figure 2. Region of study and coordinate axes (in km) of the inversion grid. Blue and red triangles represent the ALFA08 (2008–2009) and ALFA09 (2009–2010) weak-motion sensor temporary deployments, respectively. Red triangles with thick outlines mark seismographs recording during both deployments. The black triangle in the west represents GeoNet permanent station WVZ in the Waitaha river valley. Smaller black triangles represent stations of the 1994 SAPSE and Arthur's Pass aftershock deployments. The red star denotes the epicenter of the 1994 M_W 6.7 Arthur's Pass earthquake [*Bannister et al.*, 2006]. Thin gray lines represent mapped faults [*Cox and Barrell*, 2007; *Simon et al.*, 2002].

focused on a 30 by 30 km area within the ALFA08 perimeter. The ALFA09 array comprised 10 short-period instruments and recorded from October 2009 to October 2010, with ∼5 km station spacing.

The available station spacing and the relatively high rates of seismicity in the study area allow for precise hypocenter locations and high-resolution analysis of seismic properties within the array; we detected about 1380 earthquakes within and around the array for the October 2009 to May 2010 period of ALFA09 alone (dark gray circles in Figure 3). The larger station spacing of ALFA08 allows for deeper sampling of the crust, at the expense of the event detection threshold. Therefore, for the time period spanned by the ALFA08 array we examine only those earthquakes recorded by the New Zealand National Seismic Network, operated by GeoNet (http://www.geonet.org.nz; light gray circles in Figure 3). Initial hypocenter locations of both data sets were refined by manually repicking all P and S arrivals, and relocating earthquakes with a 1-D model based on results from the nearby SIGHT Transect 1 [*Van Avendonk et al.*, 2004], before subsequent relocation using the 3-D New Zealand velocity model described below.

For more detailed tomographic analysis, we selected 252 ALFA08 and 1048 ALFA09 earthquakes, excluding those with fewer than 10 associated phase picks or with epicenters greater than 20 km from the nearest seismometer. In addition, we included data for 158 aftershocks of the 1994 Arthur's Pass earthquake [*Bannister et al.*, 2006; *Robinson and McGinty*, 2000] and 129 earthquakes recorded in 1995–1996 during SAPSE (the Southern Alps Passive Seismic Experiment) [*Leitner et al.*, 2001], which provided denser ray coverage to the northeast and the southwest of our study region, respectively. The final data set for seismic tomography analysis consisted of 1648 earthquakes.
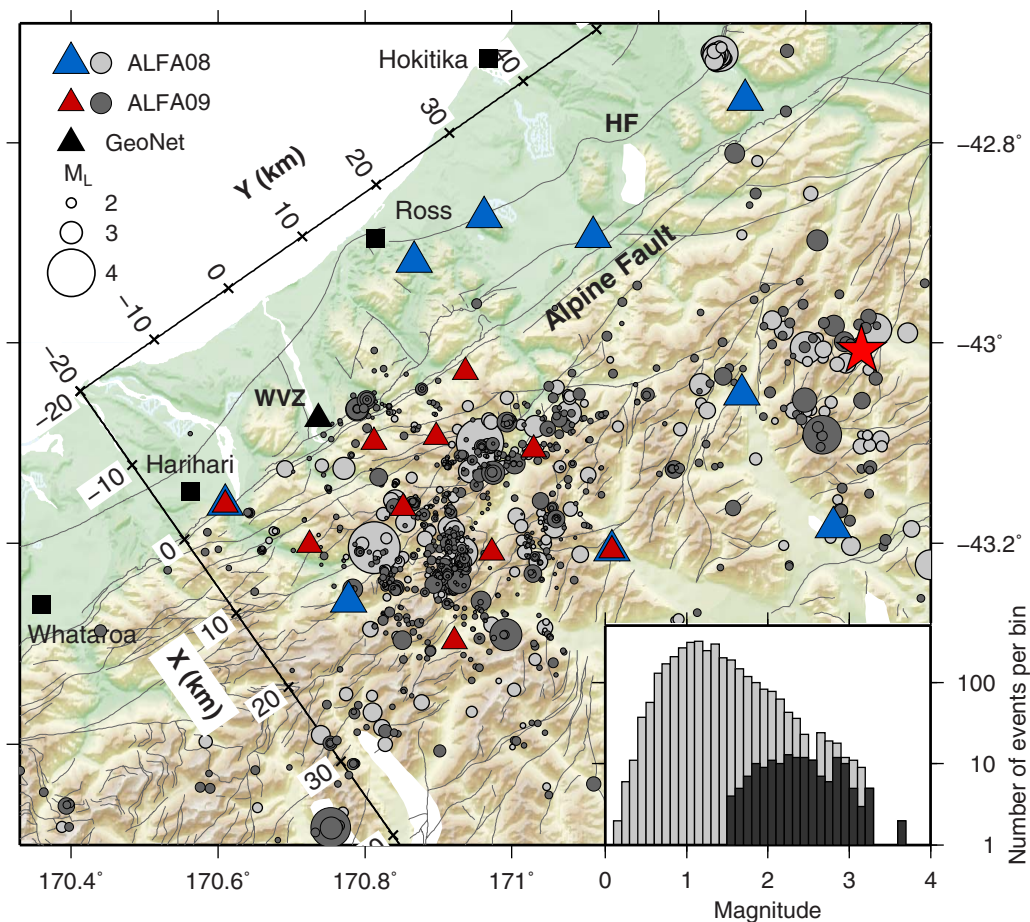
Figure 3. ALFA08 and ALFA09 temporary seismic arrays and seismicity. Blue and red triangles represent the ALFA08 (2008–2009) and ALFA09 (2009–2010) weak-motion sensor temporary deployments, respectively. Red triangles with thick outlines mark seismographs recording during both deployments. The black triangle represents GeoNet permanent station WVZ in the Waitaha river valley. Light gray filled circles are earthquakes initially detected by GeoNet then relocated using ALFA08 data and three-dimensional (3-D) Vp and Vp/Vs models. Darker gray filled circles represent 6 months of earthquakes detected and located using ALFA09 data and the same 3-D velocity models. Thin gray lines represent mapped faults [*Cox and Barrell*, 2007; *Simon et al.*, 2002]; HF: Hohonu fault. The red star on the right shows the GeoNet hypocenter location of the 18 June 1994 M_W 6.7 Arthur's Pass earthquake [*Bannister et al.*, 2006]. Black squares mark Hokitika, Ross, and Harihari townships. Lower right: magnitude-frequency distribution between November 2009 and May 2010. The dark gray bars represent earthquakes from the GeoNet catalog used to scale the ALFA09 earthquake magnitudes. Axes show the inversion grid coordinates.

2.2. Velocity Tomography Method

We use the seismic tomography method *tomoDDSP* [*Zhang and Thurber*, 2003; *Zhang et al.*, 2009] to jointly invert for hypocenters and seismic properties Vp, Vs, and Vp/Vs. The algorithm incorporates the double-difference method [*Waldhauser*, 2001], which uses event pair differential times to constrain the relative locations of hypocenters. Differential times assist with the resolution of fine structure of seismic properties near the earthquakes.

Catalog-derived differential times were calculated for all pairs of events separated by less than 20 km, resulting in an average 7 km offset between event pairs and 681608 P, 292149 S, and 280029 S-P differential times, in addition to the 18010 P, 10165 S, and 9946 S-P absolute times. These were supplemented with waveform-based differential times computed using BCSEIS, developed by *Du et al.* [2004]. The BCSEIS approach computes cross-correlation delay times in both the second-order spectral domain and the third-order (bispectrum) domain [*Nikias and Pan*, 1988; *Nikias and Raghuveer*, 1987]. Thus, by checking the consistency between cross-correlation delay times derived in the two spectral domains from both raw and filtered data, BCSEIS ensures delay time measurements are not contaminated by either Gaussian noise sources or cycle skipping [*Du et al.*, 2004].

Table 1. Hypocenter Parameters and Magnitudes of Earthquakes in the Footwall of the Alpine Fault[a]

evid	yyyy	mm	dd	hh	min	sec	Latitude (°)	Longitude (°)	z (km)	M_L
1	2009	1	8	2	43	39	−43.12043	170.68429	6.4	2.7
2	2009	2	24	22	50	40	−43.06268	170.76906	5.6	2.7
3	2010	2	27	8	6	15	−43.06650	170.78874	10.5	3.1
4	2010	2	28	10	18	35	−43.06609	170.78870	10.5	3.0
5	2010	3	25	4	49	48	−43.05708	170.80146	7.7	2.8
6	2010	3	28	10	46	8	−43.06754	170.81413	7.0	2.4
7	2010	3	30	1	39	10	−43.05719	170.80272	7.7	1.9
8	2010	4	30	16	16	21	−43.06566	170.79774	4.9	2.0

[a]Hypocenter parameters and estimated local magnitudes of earthquakes referred to as events 1–8 in Figure 12 in the footwall of the Alpine Fault for which focal mechanisms have been determined (Table 2).

The initial starting velocity model used for the *tomoDDSP* inversion is the current New Zealand-wide 3-D velocity model [*Eberhart-Phillips et al.*, 2010], which we interpolated onto a nonuniform 3-D inversion grid. The *Y* axis of this grid is oriented at N55°E, parallel to the average strike of the Alpine Fault, and the *X* axis is oriented perpendicular to the strike of the fault at N145°E (Figure 2). The initial Vs model is derived from the ratio of the New Zealand-wide Vp and Vp/Vs models.

We derived the final Vp, Vs, and Vp/Vs models using gradational inversions with increasingly fine spacing of the inversion nodes, an approach which has been found in other tomography studies to provide a reliable solution [*Eberhart-Phillips and Michael*, 1993]. The first and third inversion runs used lateral (vertical) node spacings of 10 km (4 km) and 3 km (2 km) within the ALFA09 array, respectively, with coarser spacing outside the array. The input velocity models for the second and third inversion sets were derived by averaging the Vp, Vs, and Vp/Vs solutions from inversions on staggered grids following the approach of *Haberland et al.* [2009] to ensure that poorly resolved nodes, that might become unstable in successive inversions, did not deviate significantly from the starting model. Finally, the Vp, Vs, and Vp/Vs solutions from the third inversion set were averaged and interpolated onto a new grid with minimum lateral and vertical node spacings of 2 km. In each of the second and third inversions, the starting Vs model used was that derived in the previous inversion set.

Each inversion involves first resolving the coarse velocity structure by assigning large weights to absolute travel times in the initial iterations and then refining the solution in subsequent iterations by gradually increasing the weights of differential times relative to those of absolute travel times.

The improvement to the velocity models is apparent in the overall decrease in P and S travel time residuals and the more symmetrical distributions of the final residuals compared to the initial residuals (supporting information Figure S2). The final P and S catalog time residuals have normal distributions with standard deviations of 0.06 and 0.07 s, respectively.

2.3. Hypocenter Relocation and Focal Mechanism Estimation

We relocated 1380 ALFA08 and ALFA09 earthquakes using the final 3-D Vp, Vs, and Vp/Vs models, using both absolute and differential times. After relocation, 148 focal mechanisms for a subset of well-resolved hypocenters were computed using the HASH algorithm of *Hardebeck and Shearer* [2002] applied to first-motion polarities (Tables 1, 2, and S1). In this approach, first-motion polarities are predicted for various double-couple focal mechanisms assuming a range of hypocenters consistent with the location uncertainties and the corresponding takeoff angles computed with user-defined input velocity models and compared with the observed first-motion polarities. The HASH solution and uncertainty are determined from the subset of strike, dip, and rake combinations whose predicted polarities fit a user-defined minimum fraction of observations [*Hardebeck and Shearer*, 2002].

2.4. Resolution Analysis

We have investigated the reliability of our tomographic images via a synthetic recovery test [e.g., *Eberhart-Phillips and Reyners*, 2012]. The recovered solution is an indication of how much of the initial velocity anomalies' shapes and amplitudes can be recovered by the tomographic inversion. Hence, such tests are used to highlight regions of the solution where resolution is low and seismic anomalies are smeared. The recovered synthetic anomalies may however not accurately map the resolved areas as raypaths will deviate

Table 2. Focal Mechanism Parameters for Table 1 List of Events[a]

evid	Nodal Plane 1			Nodal Plane 2			$\sigma 1$	$\sigma 2$	nppl	mfrac	qual	stdr
	str (°)	dip (°)	rake (°)	str (°)	dip (°)	rake (°)						
1	43	49	−177	311	88	−41	16	27	11	0.1	A	0.39
2	239	55	113	23	41	61	22	22	10	0.1	A	0.38
3	172	71	79	22	21	119	23	33	11	0.0	B	0.65
4	39	20	117	191	72	81	13	14	13	0.0	A	0.62
5	98	14	180	188	90	76	6	11	13	0.0	A	0.59
6	189	73	62	70	32	147	16	23	11	0.0	A	0.58
7	158	84	55	60	36	170	13	27	11	0.0	A	0.58
8	1	85	−67	103	23	−167	13	16	11	0.0	A	0.48

[a]Focal mechanisms were determined from first motion polarities and the HASH software [*Hardebeck and Shearer*, 2002]. Columns contain the event number and HASH output parameters including the strike, dip, and rake of the two focal planes; $\sigma 1$ and $\sigma 2$: angular uncertainties of the normals to the focal planes; nppl: the number of first motion polarities; mfrac: the weighted fraction misfit of first motions; qual: the HASH-rated quality on a scale of A to F; stdr: the station distribution ratio (0–1, where stdr $<$ 0.5 indicates that a relatively large number of data lie near nodal planes). Further description of these parameters can be found in the HASH software manual [*Hardebeck and Shearer*, 2002]. Both the mfrac and stdr parameters are defined as in the FPFIT software [*Reasenberg and Oppenheimer*, 1985]. We used two input 1-D velocity models to represent the range of values of our Vp solution (Figure 6). Based on these input models, HASH estimates a range of trial takeoff angles from which to compute focal mechanisms.

from the real case due to the velocity model being different from reality. The synthetic recovery test (supporting information Figure S3) used the solutions from subsequent inversions on staggered grids with minimum horizontal node spacings of 5 and 3 km.

As expected, the test indicates that the resolving power of our inversion is highest within the central part of the ALFA09 array, coinciding closely to areas in which the derivative-weighted-sum (DWS) values exceed 100. The DWS [*Scales*, 1989; *Toomey and Foulger*, 1989] is an average relative measure of the density of seismic rays near a given node, but is independent of the angular distribution of seismic raypaths. Within this central region (X-grid distances of −2 to 25 km, Y-grid distances of −10 to 25 km, and depths of 1–10 km), up to 90% of the synthetic Vp and Vs anomalies are recovered. Vp/Vs anomalies are less well resolved due to the larger error associated with the synthetic t_S-t_P times, and the need for both the *P* and *S* wave arrivals to be present for a particular earthquake-station pair. Up to 40–80% of Vp/Vs anomalies are recovered above 6 km depth but resolution decreases below that depth. Outside of this central region, however, large-scale longer wavelength structures have already been resolved as part of the work undertaken to develop the New Zealand-wide 3-D model [*Eberhart-Phillips and Bannister*, 2002; *Eberhart-Phillips et al.*, 2010], as well as by the previous set of inversions on the coarser grid with 10 km node-spacing. In this regard, lower DWS values in the final high-resolution grid do not fully reflect the resolution obtained with the iterative, staggered-grid inversion approach.

We have also performed a ray density tensor analysis [*Kissling*, 1988] to determine regions of the solution likely to be biased, smeared or poorly resolved due to uneven angular distributions of rays or to low ray density. Our analysis (Figures 4 and 5) shows that beneath each station of the array, rays down to ~2 km depth are predominantly subvertical. At Y-grid distances of −5 to 5 km and X-grid distances up to 10 km, the P and S rays predominantly plunge southeast (Figure 5) and trend perpendicular to the strike of the Alpine Fault (Figure 4). Finally, around 5 km depth in the Vp model and down to about 15 km depth in the Vs and Vp/Vs models, seismic rays are predominantly subhorizontal (Figure 5).

3. Results

3.1. Seismic Tomography Results

The long-wavelength features of the Vp, Vs, and Vp/Vs solutions (Figure 6) are broadly similar to those of the New Zealand-wide 3-D velocity model [*Eberhart-Phillips et al.*, 2010], but generally strike more parallel to the Alpine Fault. At 3 km depth, the Vp and Vs solutions (Figure 6) exhibit faster wave speeds in the north of the model and slower wave speeds in the southwest and southeast within 10–20 km of the Alpine Fault trace. The Vp/Vs solution shows lower Vp/Vs values northwest of an X-grid distance of ~10 km and higher values to the southeast. These variations result in a locally more pronounced and elongated low Vp/Vs anomaly than in the initial model. At 6 km depth, both Vp and Vs solutions are faster overall than the initial model, while the Vp/Vs solution shows variations from the initial model similar to those at 3 km depth.
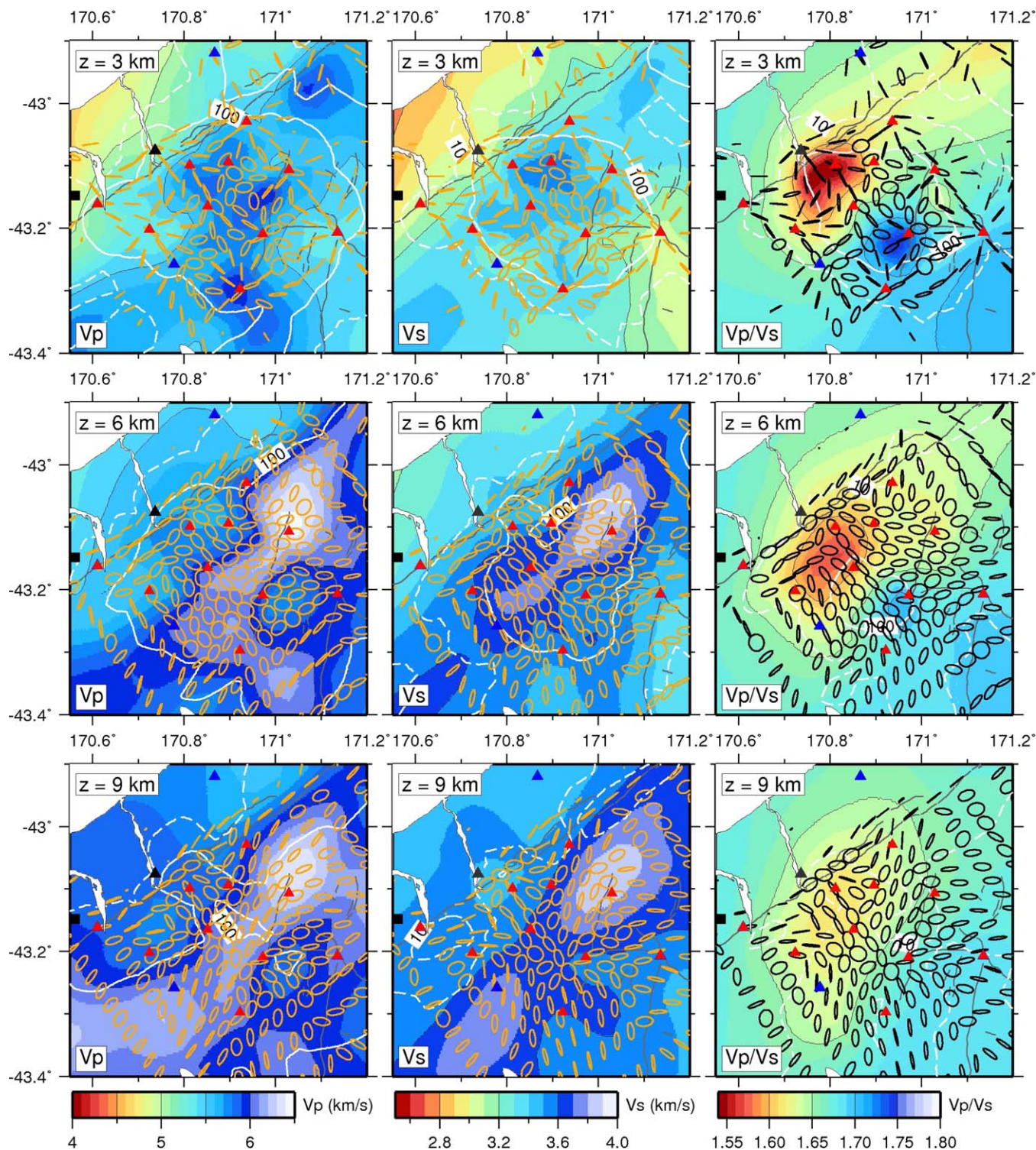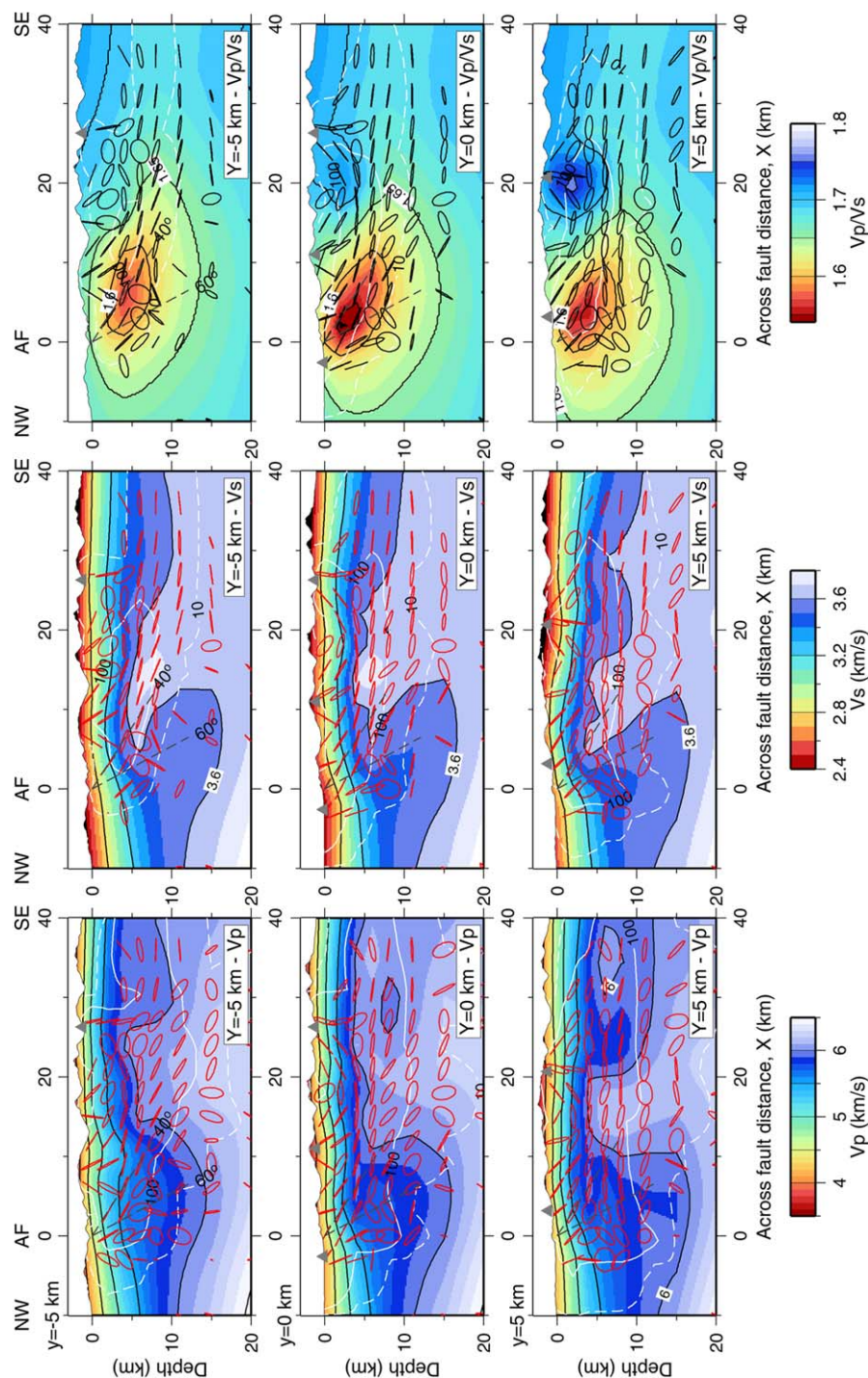
Figure 4. Ellipses representing the projection of (left) P, (middle) S, and (right) S-P ray density tensors [*Kissling*, 1988] at (top) 3 km, (middle) 6 km, and (bottom) 9 km depths onto the corresponding depth slices of the Vp, Vs, and Vp/Vs solutions, respectively. Ellipses are centered about nodes of the final inversion grid with 3 km horizontal node spacing. Solid and dashed white contours represent the ray DWS (derivative weighted sum) contours of 10 and 100. Red, blue, and black triangles represent the ALFA08, ALFA09, and the Geonet WVZ recording stations. The black square to the left denotes the township of Harihari.

Figure 5. Ellipses representing the projections of (left) P, (middle) S, and (right) S-P ray density tensor [*Kissling*, 1988] ellipsoids onto the vertical slices of the Vp, Vs, and Vp/Vs solutions, respectively. Ellipses are centered about nodes of the corresponding final inversion grids with 3 km horizontal node spacing. Solid and dashed white contours represent the ray DWS (derivative weighted sum) contours of 10 and 100. Gray triangles represent recording stations within a 3 km distance of the cross section. Dashed lines show extrapolations of a 40 and 60°-dipping Alpine Fault.
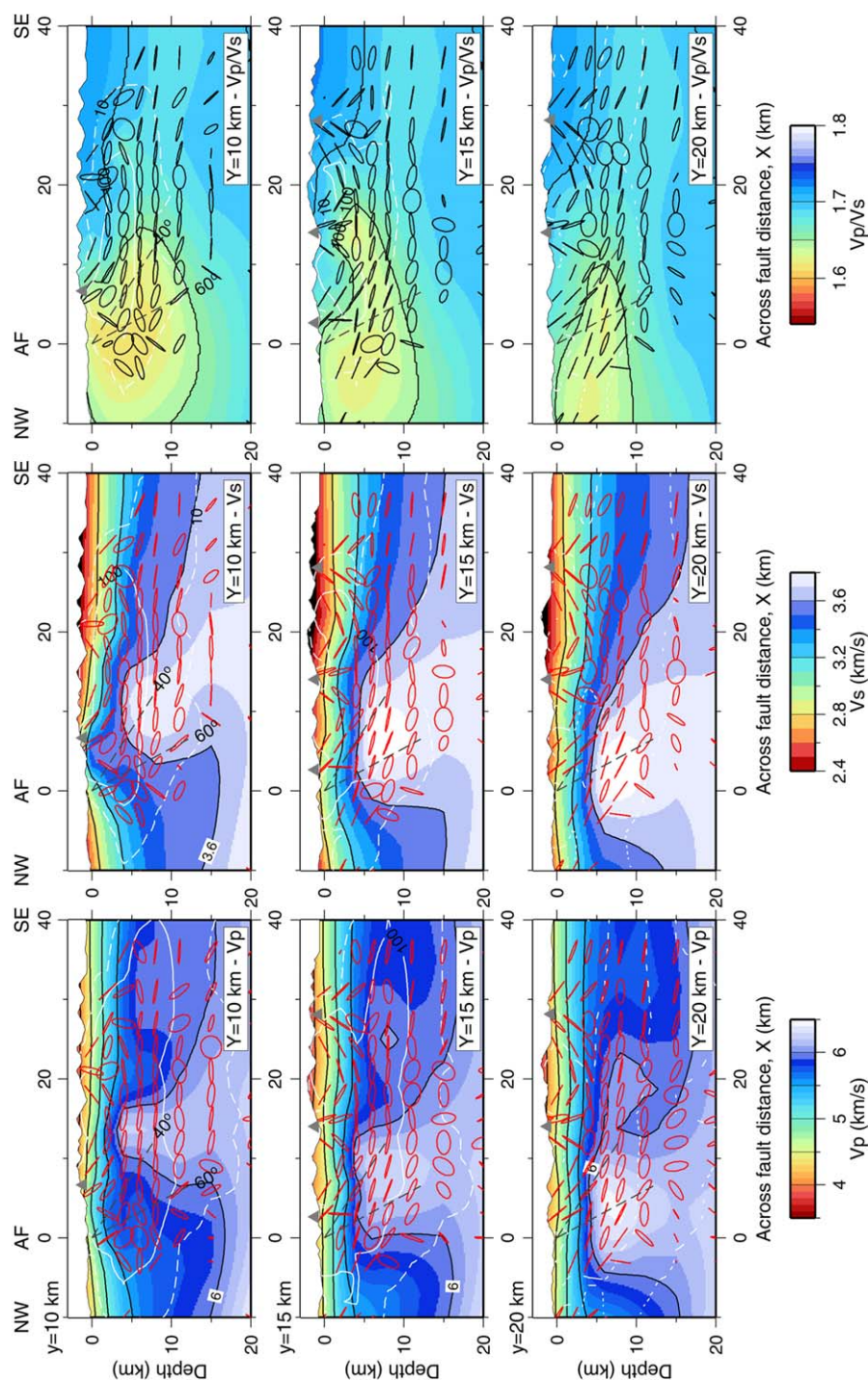
Figure 5. (Continued)
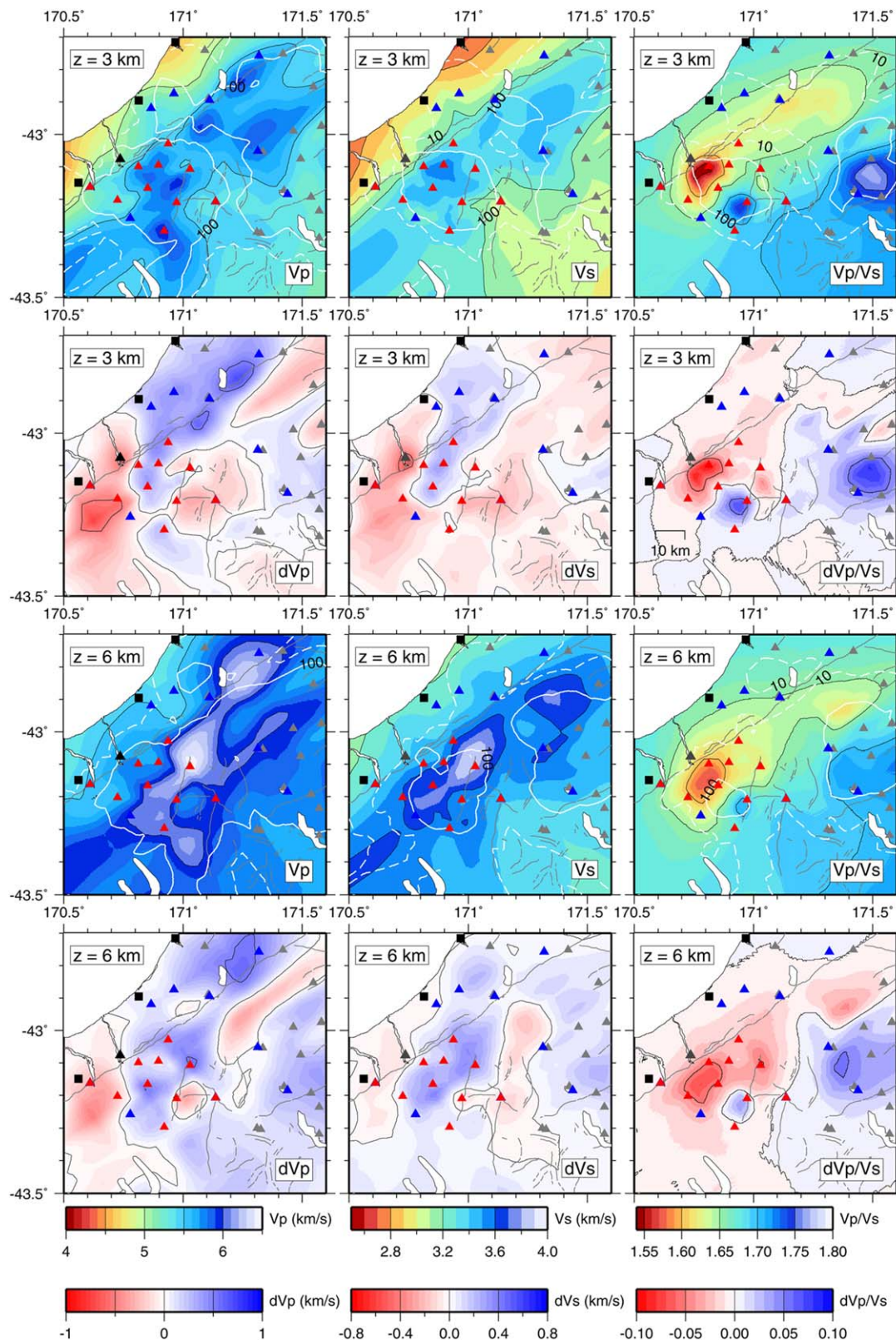
Figure 6. Horizontal slices through the (left) Vp, (middle) Vs, and (right) Vp/Vs models at 3 km, 6 km and 9 km depths and their deviations from the initial model. The black squares from north to south denote the positions of Hokitika, Ross, and Harihari. Blue, red, black, and gray triangles represent ALFA08, ALFA09, GeoNet WVZ, and the 1994 SAPSE and Arthur's Pass aftershock recording stations. Note that the westernmost and easternmost red triangles correspond to stations occupied in both ALFA08 and ALFA09 experiments. Solid and dashed white contours represent ray DWS (derivative weighted sum) values of 100 and 10, respectively. Gray lines represent the Alpine Fault and major faults in the area.
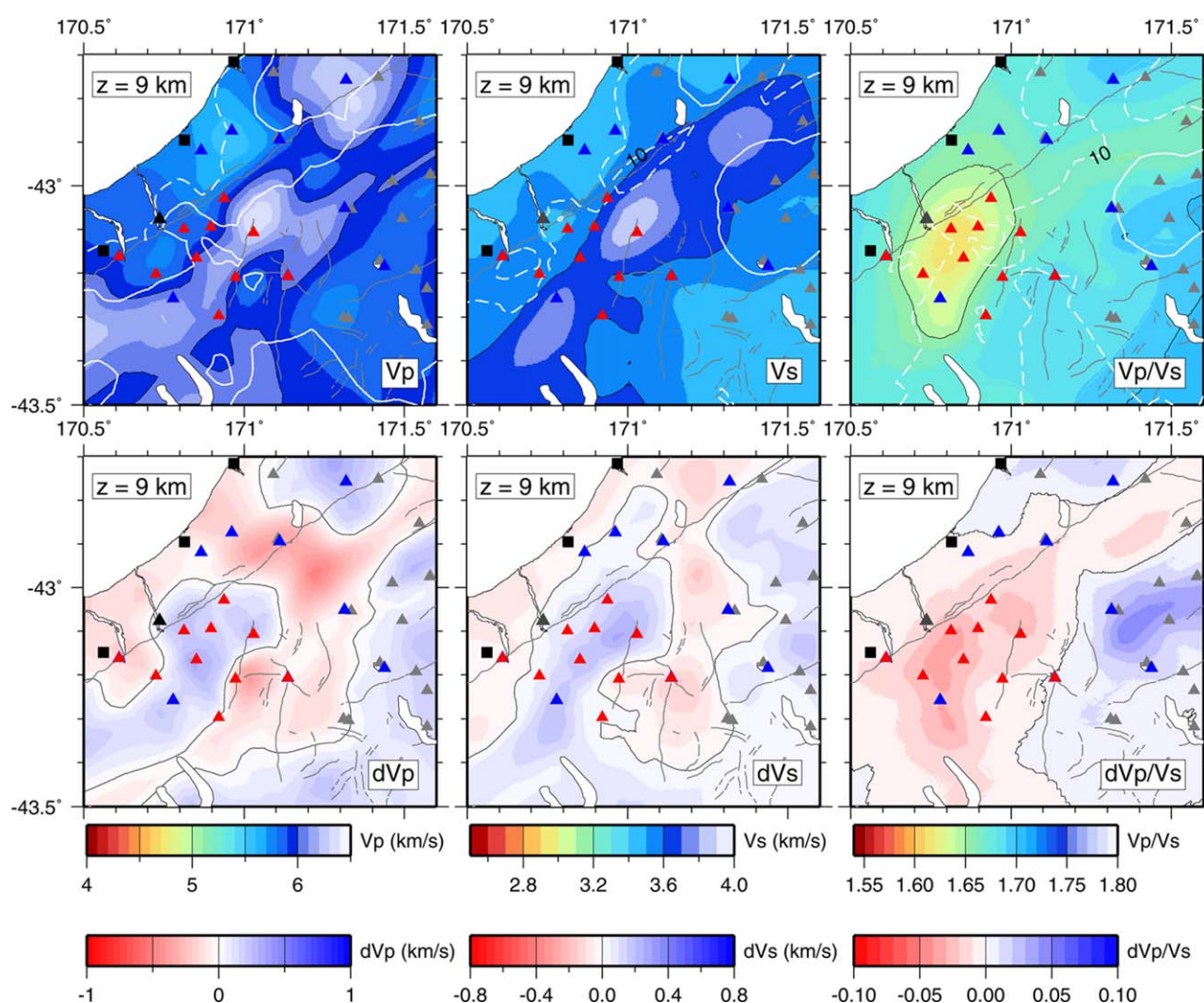
Figure 6. (Continued)

Below, we describe the main features of the tomographic results in horizontal slices (Figure 6) and a vertical slice (Figure 7) through the center of the final solution model at a Y-grid distance of 5 km (Figure 2). Other cross sections through the final model are provided in supporting information Figure S5.

The most pronounced feature of the tomographic results is a ~10 km wide tongue of high-Vp and high-Vs doming at 3–5 km depth below the highest topography (X = 10–20 km; Figure 7), perhaps representing uplifted material. The Vs anomaly extends ~5 km further west than the Vp anomaly, toward the trace of the Alpine Fault, suggesting a relationship to a dipping structure. The high-velocity tongue is bordered in the west by a zone (X-grid of −5 to 10 and 5–15 km depth) in which Vp and Vs contours are ~5 km deeper than to the southeast (X ~ 40 km). The transition from the zone of low Vp and low Vs to the high-velocity tongue results in a sharp lateral gradient.

At 5 km depth, for example, the Vp values increase by ~8% from 5.7 km/s (northwest of the X-grid 10 km) to 6.2 km/s (southeast of X = 10 km), and Vs values increase by 6%, from 3.4 to 3.6 km/s. Laboratory measurements on rock samples [*Christensen and Okaya*, 2007] suggest that this lateral increase in Vp and Vs can be reasonably explained by a transition in lithology from Alpine Fault mylonites and garnet or biotite schist to Torlesse greywacke. However, as the mylonite zone is only of the order of 1 km in width, it is unlikely that its effects can be detected using the methods employed here. Moreover, geological cross sections [*Cox and Barrell*, 2007] indicate schist at ≥5 km depth extending as far as 20 km southeast of the Alpine Fault
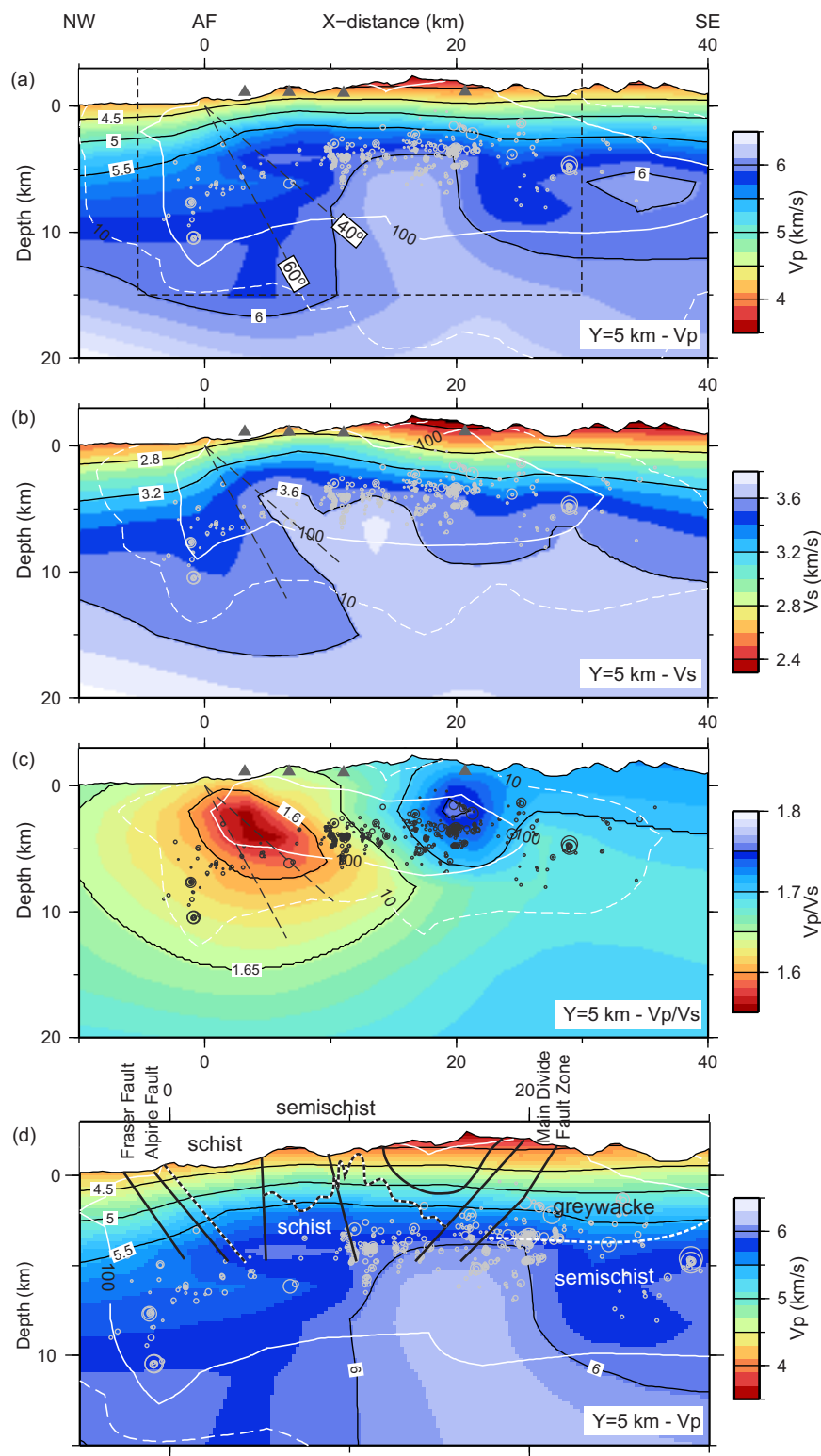
Figure 7. Vertical slice perpendicular to the Alpine Fault (Y-grid distance of 5 km) through the solution models with (a) Vp solution; (b) Vs solution; (c) Vp/Vs solution; (d) adapted geological cross section along the Waitaha Valley [*Cox and Barrell*, 2007] superimposed onto the Vp solution. The dashed square box in Figure 7a shows the extent of cross section of Figure 7d. Shown hypocenters are within 5 km of the cross section and have estimated horizontal and vertical uncertainties less than 1 km (see supporting information S1). Solid and dashed white contours represent ray DWS (derivative weighted sum) of 100 and 10, respectively. Short white dashes in Figure 7d represent the boundary between greywacke and semischist. Short black and white dashes represent boundaries between semischist and schist or schist and mylonite next to the dipping Alpine Fault.
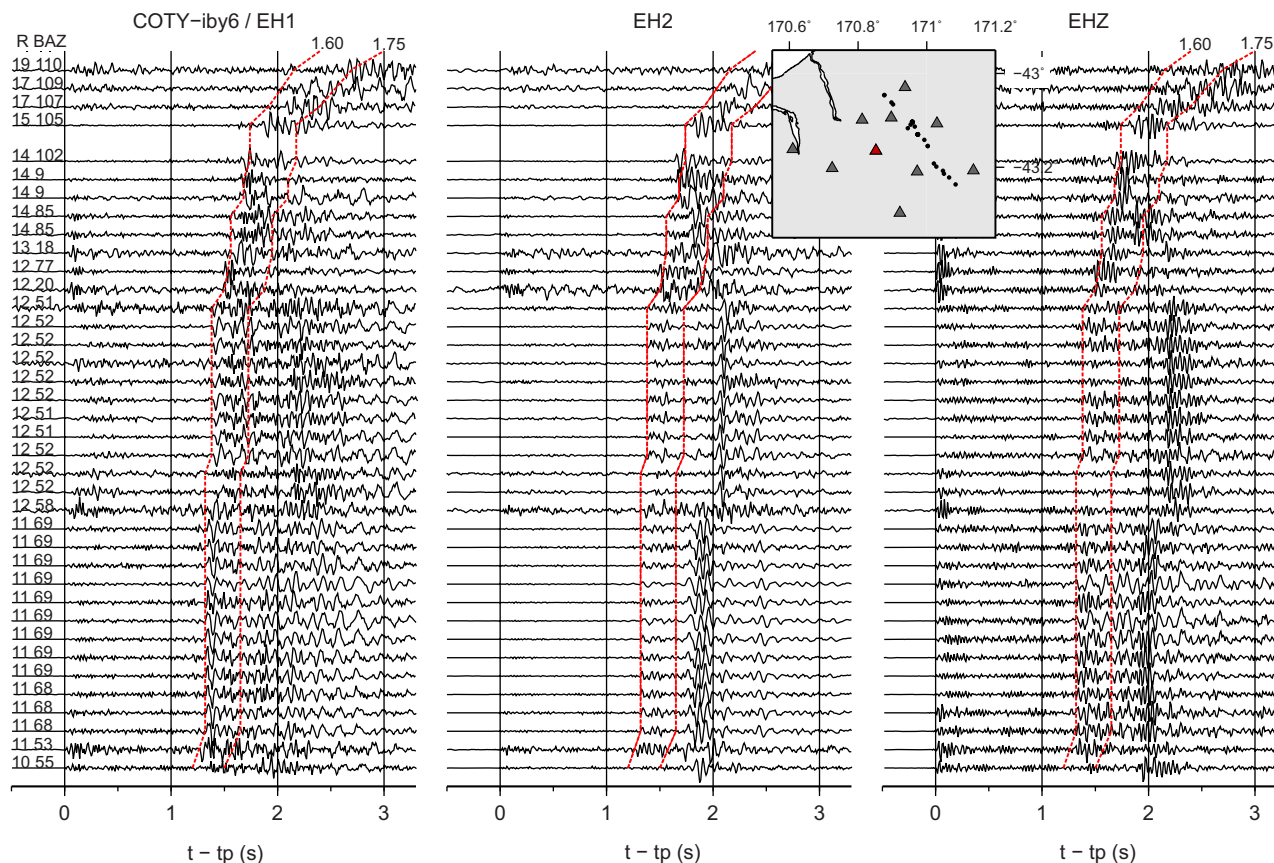
Figure 8. Horizontal (EH1 and EH2) and vertical (EHZ) recordings of earthquakes at the ALFA09 station COTY located 11 km southeast of the Alpine Fault. Parameters R and BAZ to the left of the figure indicate event hypocentral distances and back azimuths. Horizontal components are rotated to 55° (EH1) and 145° (EH2) parallel and perpendicular to the Alpine Fault, respectively. Time is in seconds after the P arrival. The red dashed lines show the expected S-P travel times for an assumed P wave speed of 4.5 km/s and Vp/Vs ratios of 1.60 and 1.75. Note shear wave delay times of ∼0.7 s at the hypocentral distance of ∼12 km and back azimuths of ∼52°. Top: map showing the COTY station as a red triangle and selected earthquake epicenters as black dots.

(Figure 7d). An alternative cause of the apparent lateral gradients may be the strong P and S seismic anisotropy of up to 20 and 26% reported for the Alpine Schist [*Christensen and Okaya*, 2007]. Seismic anisotropy could account for the 8% Vp variation described above if there were a change in the schist foliation from dipping to horizontal ∼10 km southeast of the Alpine Fault, given that the majority of raypaths are horizontal in this region (Figure 5). Finally, the presence of fluid-filled pores in the midcrust inferred from magnetotelluric data [*Wannamaker et al.*, 2002] ∼25 km south of this study could substantially decrease both Vp and Vs [e.g., *O'Connell and Budiansky*, 1974; *Takei*, 2002].

West of the high-velocity tongue lies a ∼20 km wide 0–15 km deep zone of low Vp/Vs (1.60–1.65), adjacent to and southeast of the Alpine Fault trace. The extent of this feature to the southwest of the ALFA09 array cannot be determined. Vp/Vs ratios of 1.60–1.65 are atypically low for the garnet and biotite schists (mean Vp/Vs ≥ 1.69 measured on dry samples [*Christensen and Okaya*, 2007]) expected here [*Cox and Barrell*, 2007]. In contrast, southeast of an X-grid distance of 20 km, Vp/Vs ratios in the range 1.68–1.75 are characteristic of the schist and Torlesse greywacke [*Christensen and Okaya*, 2007].

Within the zone of low Vp/Vs ratios, there is a small zone with even lower Vp/Vs values of 1.55–1.60 (X = 0–10 km, Y = −10 to 10 km at <7 km depth; Figures 6 and 7c). This zone dips southeast from the surface trace of the Alpine Fault at approximately 45°. The raypath density analysis (Figures 4 and 5) suggests that Vp/Vs values in this zone are likely biased by the uneven ray distribution, as the wave propagation directions here are predominantly inclined to the southeast and mostly perpendicular to the Alpine Fault. Seismic waveforms at stations in the ALFA09 array consistently show two distinct S arrivals of similar amplitudes separated by up to 0.7 s (Figures 8, 9, and S6), which we attribute to seismic anisotropy in the schist. As the
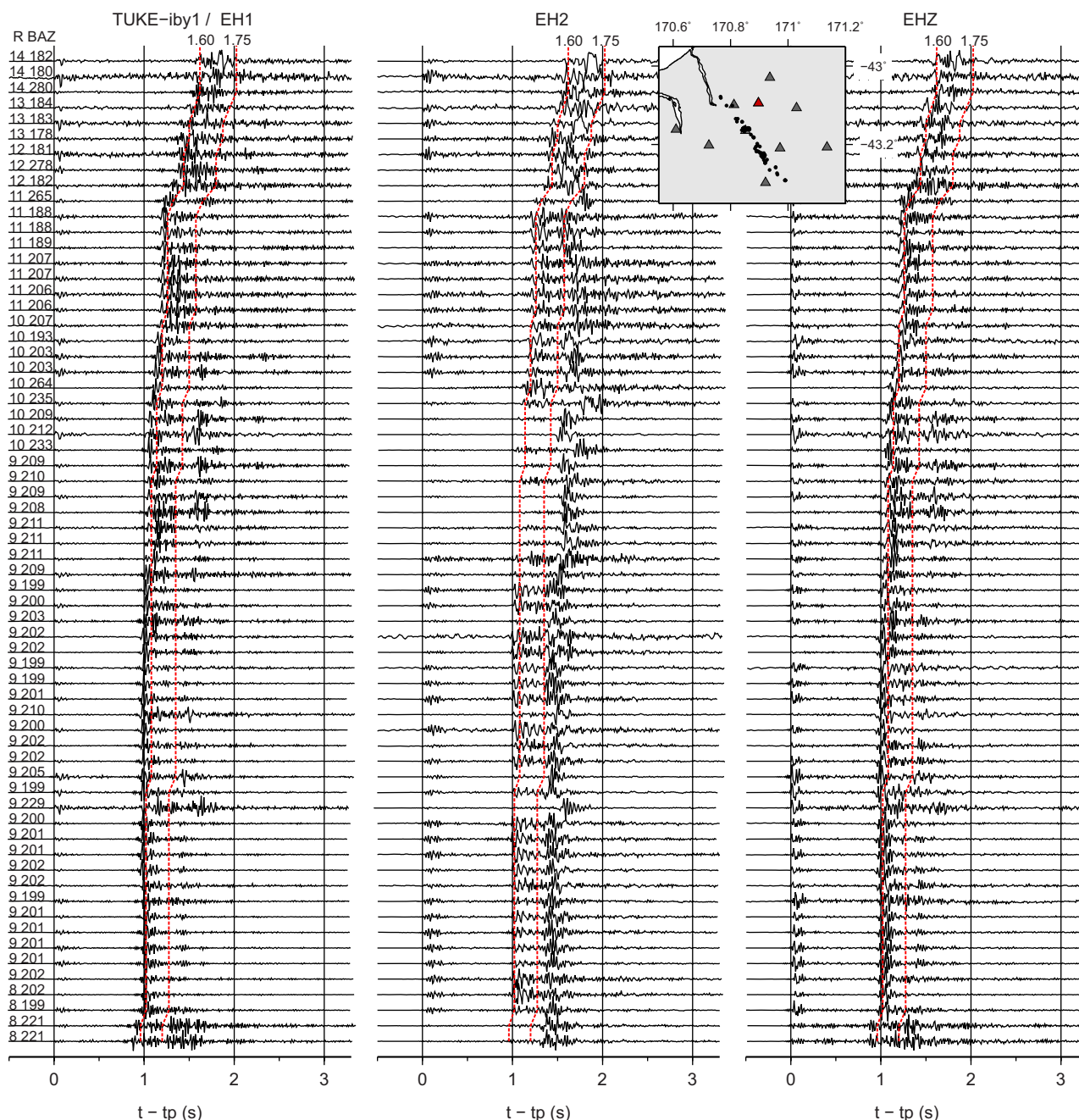
Figure 9. Horizontal (EH1 and EH2) and vertical (EHZ) recordings of earthquakes at the ALFA09 station TUKE located 6 km southeast of the Alpine Fault. Parameters R and BAZ to the left of the figure indicate event hypocentral distances and back azimuths. Horizontal components are rotated to 55° (EH1) and 145° (EH2) parallel and perpendicular to the Alpine Fault, respectively. Time is in seconds after the P arrival. The left columns indicate the hypocentral distance R and the station-event back azimuth. The red dashed lines show the expected S-P travel times for an assumed P wave speed of 4.5 km/s and Vp/Vs ratios of 1.60 and 1.75. Note shear wave delay times of ∼0.5 s at hypocentral distances of 9–10 km and back azimuths of ∼211°. Top: map showing the TUKE station as a red triangle and selected earthquake epicenters as black dots.

picking methodology we employ identifies the first and therefore faster S arrival, S wave anisotropy is likely to bias the Vs solution toward higher values, and the Vp/Vs model toward lower values. In the region where Vp/Vs values are in the range 1.55–1.60, the predominant ray orientation is likely to be the reason for the very low Vp/Vs values. Accordingly, the low Vp/Vs values cannot be interpreted unambiguously to be due to the presence of a fluid or gas phase. In the same region, the Vs solution shows an inclined zone with high values that may result from the uneven ray distribution.
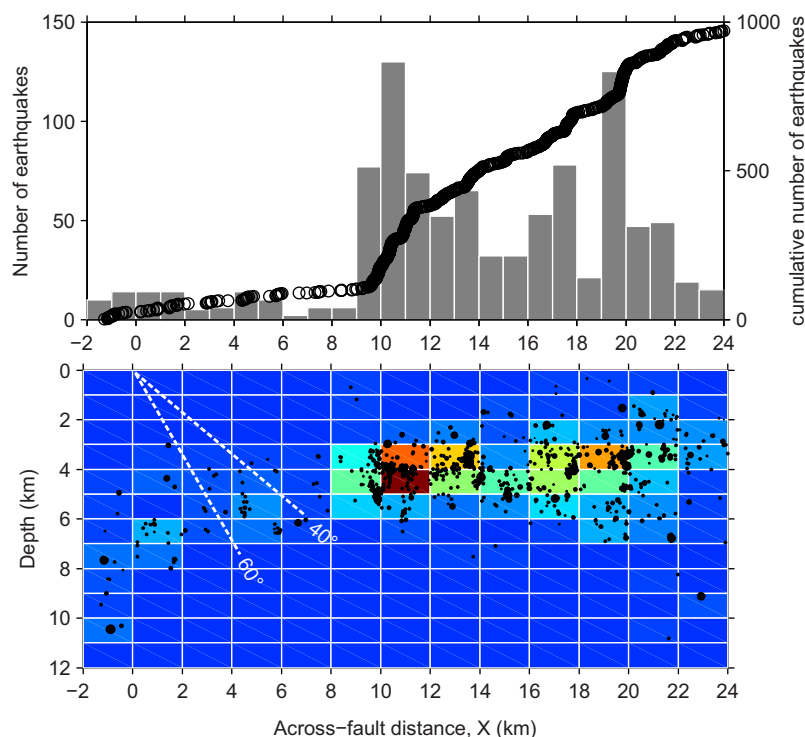
Figure 10. (top) Frequency (histogram) and cumulative number (circles) of earthquakes as a function of the model coordinate X. Selected earthquakes were recorded during the 2009–2010 period of ALFA09 and located within the ALFA09 array (model coordinates X = −2 to 24 km and Y = −15 to 20 km) with a hypocenter depth error less than 2 km. (bottom) Two-dimensional histogram showing earthquake frequency with respect to the model coordinate X and depth. Black circles represent single hypocenters projected onto the depth section and scaled with respect to the earthquake magnitude. Dashed white lines show depth extrapolations of a 40 or 60°-dipping Alpine Fault.

The zone of Vp/Vs = 1.70–1.75 centered on X = 20 km, Y = 0 km, and a depth of ∼3 km (Figure 7c) is confined directly beneath a seismometer station and hence is likely biased by the predominantly vertical ray orientation directly beneath that station (Figure 5).

3.2. Seismicity Distribution

The completeness magnitude we obtain within the region spanned by the ALFA09 array during the recording period of the ALFA08 and ALFA09 arrays is ∼1.5 (Figure 3). This is about one magnitude unit lower than the GeoNet earthquake catalog completeness magnitude for this region, of ∼2.7 [*O'Keefe*, 2008], due primarily to the dense station spacing of the ALFA09 array, which results in enhanced detection and location. A similar completeness magnitude to ours was achieved for the SAMBA array with a station spacing of approximately 8 km [*Boese et al.*, 2012, Figure 8].

Hypocenter depth errors are estimated to be ≤0.6 km (see supporting information S1), giving us confidence that differences >1 km in the depth of the seismic-aseismic transition are real.

Overall, little seismicity is observed within 9 km of the Alpine Fault (Figures 3 and 7), with the exception of a cluster of earthquakes that occurred in late 2008 and included a magnitude M_L ∼ 3.6. This cluster was located 2–3 km northwest of the Alpine Fault trace (Figure 3) and is likely in the Hohonu Batholith [*Waight et al.*, 1997]. We analyze the variations in seismicity density with proximity to the Alpine Fault trace in more detail below.

3.2.1. Within 2 km West of the Alpine Fault Trace

Within the 6 month period of the ALFA09 array, 25 earthquakes occurred within 2 km west of the Alpine Fault, at depths of 4–11 km depth (Figures 10 and 11). This depth range is similar to that determined by *Boese et al.* [2012] using data from the SAMBA array 40–100 km southwest of our study area. Seven of these earthquakes occurred directly north of the Waitaha River (near GeoNet seismometer station WVZ in Figure
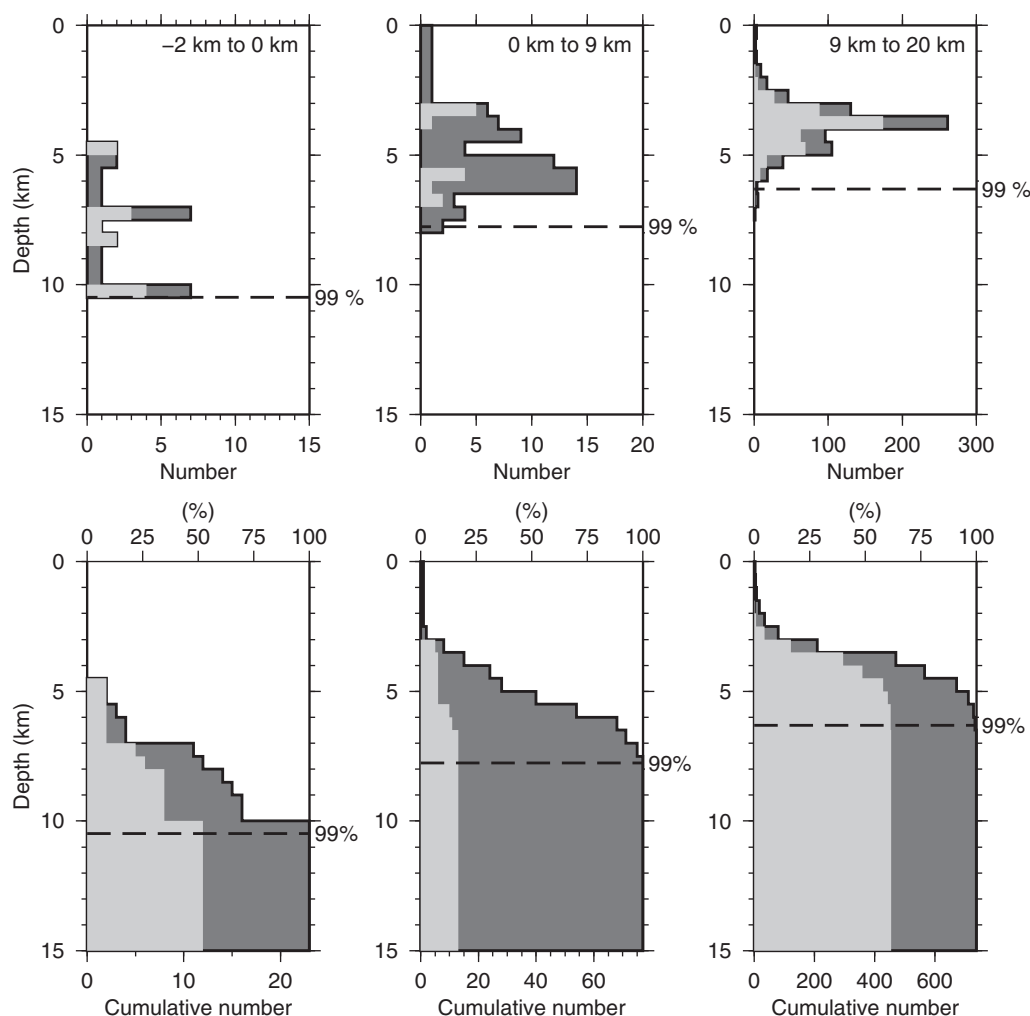
Figure 11. (top) Depth distribution and (bottom) cumulative number of hypocenter locations of earthquakes recorded during the 2009–2010 period of ALFA09 and located within the ALFA09 array (model coordinates X = −2 to 20 km and Y = −15 to 20 km) with an hypocenter depth error less than 2 km. Dark gray bars represent hypocenters within the X distance range specified at the top of each graph. Light gray bars represent the portion of hypocenters with a depth uncertainty (1σ) less than or equal 0.1 km (see supporting information S1).

3) and had estimated local magnitudes of between 1.9 and 3.1. Focused activity in this area was also apparent in the earlier microseismicity study of *O'Keefe* [2008].

The focal mechanisms of earthquakes occurring near the trace of the Alpine Fault are not particularly well constrained (angular uncertainty of the normal to the nodal plane 1$\sigma \leq 33°$), but the mechanisms for three of the largest and highest-quality ("A") earthquakes (focal mechanisms 4–6 in Figure 12 and Tables 1 and 2) consistently indicate reverse slip on either a steeply northwest-dipping plane (strike/dip/rake of 188–191°/72–90°/73–81°) or a less well-constrained shallow southeast-dipping plane (39–98°/14–32°/117–180°). This contrasts with the focal mechanisms for the region to the southeast, which are dominantly strike slip (Figure 12 and supporting information Table S1).

3.2.2. Within 0–9 km Southeast of the Alpine Fault Trace

Seismicity is sparse between 0 and 9 km from the Alpine Fault trace on the hanging wall side (Figure 10). All the earthquakes in this area are shallower than 8 km depth within 2 km and shallower than 7 km depth within 2–9 km southeast of the Alpine Fault trace, respectively (Figure 10), and thus markedly shallower than the earthquakes occurring directly west of the trace. In particular, 56% of the earthquakes are shallower than 6 km depth. The change in the distribution of hypocenter depths appears to be abrupt, taking place within 1 km of the Alpine Fault (Figure 10) and exceeds the 0.6 km standard deviation in hypocenter depth errors (see supporting information S1).
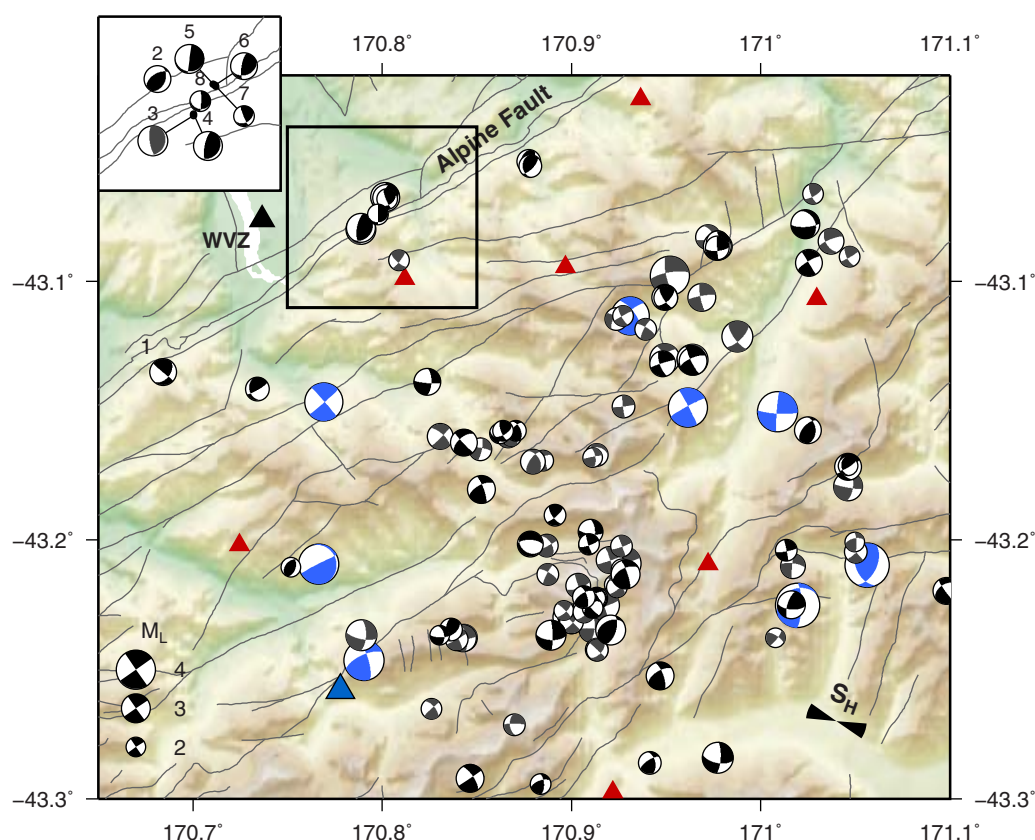
Figure 12. Focal mechanisms determined within the ALFA09 array for the period from October 2008 to May 2010 (Tables 1, 2, and S1). Focal spheres are lower hemisphere projections. Spheres with black and gray quadrants represent HASH class A and class B focal mechanisms, respectively, with a minimum of 10 first motion polarities and first motion weighted fraction misfits ≤0.1. Annotated focal mechanisms 1–8 along the Alpine Fault are listed in Table 2. Blue focal mechanisms show earthquakes occurring between 2003 and 2013 for which GeoNet determined a moment tensor solution [*Ristau*, 2008]. The bow-tie represents the regional maximum horizontal compressive stress orientation of 115 ± 10° (80% confidence level) determined by *Boese et al.* [2012].

Boese et al. [2012] commented on the low rates of seismicity associated with hanging wall schists of textural zones III and IV [*Cox and Barrell*, 2007; *Turnbull et al.*, 2001] southeast of Franz Josef (Figure 13). A similar association is exhibited by seismicity in the Harihari-Ross segment with little seismicity within 9 km of the Alpine Fault and most seismicity occurring further than ∼9 km from the fault trace in biotite greenschist or chlorite greenschist hanging wall rocks of textural zones IIB and IIA (Figure 13). Directly south of this study area between Harihari and Franz Josef, however, the 20–30 km wide region of low-seismicity spans the schist textural zones II to IV. Hence, there is no discernible correlation between the surface geology and seismicity along the central Alpine Fault with the exception of perhaps a slight widening of the textural zone IV (Figure 13).

3.2.3. Nine to Twenty Kilometers Southeast of the Alpine Fault Trace

The number of earthquakes increases dramatically beyond 9 km southeast of the Alpine Fault trace (Figure 10). More than 80% of the earthquakes recorded by the ALFA09 array occurred within a band between 9 and 20 km from the Alpine Fault. Of these, 99 and 50% are shallower than 7 and 4 km depth, respectively, with a frequency peak between 3 and 4 km depth (Figure 11). The distribution suggests that the seismic-aseismic transition in this region is 7 km deep. This depth is, within uncertainty, the same as the maximum seismogenic depths of about 8 km inferred in previous studies [*Boese et al.*, 2012; *Leitner et al.*, 2001; *Reyners*, 1988], even though those results pertained to the region 40–100 km southwest of the ALFA09 array where surface elevations and exhumation rates are higher [e.g., *Little et al.*, 2005]. The previous studies all employed approximate 1-D velocity models for hypocenter calculations, in contrast to the 3-D models used here, and with the exception of the study by *Boese et al.* [2012], had station spacings substantially larger
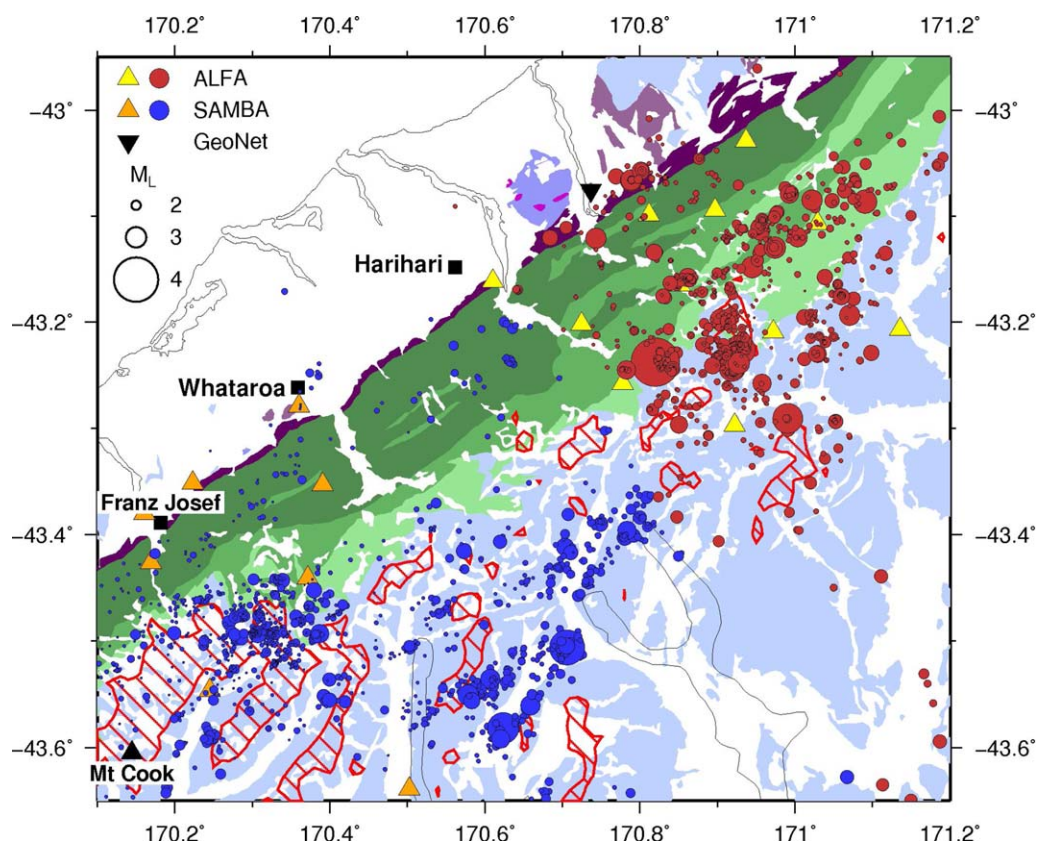
Figure 13. ALFA and SAMBA relocated seismicity and geological map of the central Alpine Fault area. Red dots represent ALFA08 (2008–2009) and ALFA09 (2009–2010) epicenters with Y-grid coordinate greater than −13 km. Blue dots represent SAMBA (2008–2010) [*Boese et al.*, 2012] epicenters with Y-grid coordinate less than −13 km. Shown hypocenters have vertical uncertainty of less than 2 km. Yellow and orange triangles indicate ALFA08/09 and SAMBA seismographs, respectively. The inverted black triangle denotes GeoNet permanent station WVZ. The background geological map is after [*Simon et al.*, 2002; *Cox and Barrell*, 2007]. The map outlines the mylonites (purple), the Alpine Schist textural zones II (semischist), III and IV (light to dark green), and the greywacke (light blue) located southeast of the Alpine Fault and batholiths (lilac) located northwest of the Alpine Fault. Red hashed shapes show elevations of 2000 m and above.

than those provided by the ALFA09 array. Thus, it appears that the depth of the seismic-aseismic transition is largely uniform for ~200 km along the central Alpine Fault, despite large changes along-strike in the maximum surface elevation, exhumation rates, and by inference the thermal regime. As noted also by *Boese et al.* [2012], maximum hypocenter depths appear to increase south-eastward beyond 20 km from the Alpine Fault trace, although hypocenters at such distances from the fault are less well constrained than those within the respective networks (supporting information Figure S1).

The relocated earthquake epicenters and hypocenters clearly show clusters of seismicity 9–20 km southeast of the Alpine Fault (Figures 3 and 10). These clusters appear associated with the leading edge of the high-Vp, high-Vs structure and to coincide closely with the projections (Figure 7d) of previously mapped surface faults [*Cox and Barrell*, 2007]. In particular, some of the clusters have an apparent NW dip (Figure 7d) and appear to be associated with faults of the Main Divide Fault Zone [*Cox and Findlay*, 1995] that strike obliquely to the Alpine Fault. We infer that these earthquakes confirm present-day seismic activity on the deep extensions of structures previously suspected to be active [*Cox et al.*, 2012]. Faults in this region, beneath the Southern Alps and east of the Alpine Fault, have been suggested to accommodate some of the remainder (10–15%) of the relative plate motion not already accommodated by coseismic slip on the Alpine Fault [*Wallace et al.*, 2006].

Focal mechanisms determined for our best-recorded events with hypocenters close to mapped surface faults indicate predominantly strike-slip movement (Figure 12) consistent with the interpretation that they represent slip on previously recognized faults. *Boese et al.* [2012] also observed a preponderance of strike-

slip mechanisms at comparable distances from the Alpine Fault trace in the region $\sim$100 km south and determined a homogeneous strike-slip stress field for the central Southern Alps with a maximum horizontal compressive stress orientation of $115 \pm 10°$, similar to that observed across much of the South Island [*Townend et al.*, 2012].

4. Discussion

As described in the previous section, the distribution of seismicity in the vertical cross section perpendicular to the strike of the Alpine Fault at Y = 5 km (Figure 7) illustrates several distinct features:

1. Sparse, relatively deep seismicity (4–11 km) directly west of the fault trace (X = −2 to 0 km), associated with Vp $\sim$ 5.5–5.9 km/s, Vs $\sim$ 3.2–3.5 km/s, and Vp/Vs < 1.65.

2. Sparse, shallower seismicity (3–8 km) within 9 km of the trace on the southeastern side of the fault (X = 0–9 km), associated with Vp $\sim$ 5.7 km/s, Vs $\sim$ 3.4 km/s, and Vp/Vs $\sim$ 1.60.

3. Abundant shallow seismicity (2–7 km) further than 9 km southeastward of the fault trace (X = 9–20 km), associated with Vp $\sim$ 6 km/s, Vs $\sim$ 3.5 km/s, and Vp/Vs $\sim$ 1.62–1.75.

We consider here how the lateral (i.e., fault-perpendicular) variations in the rate of seismicity and the seismogenic thickness may be related to lithologic, structural, or environmental conditions.

4.1. Relationships Between Seismogenic Thickness, Thermal Structure, and Deformation Rates

Similarities between earthquake depth frequency distributions and predicted yield strength envelopes have been interpreted for several decades to indicate that the seismic-aseismic transition is governed by the gradual onset of temperature and strain rate-dependent ductile deformation mechanisms of rocks [e.g., *Chen and Molnar*, 1983; *Meissner and Strehlau*, 1982; *Scholz*, 1988; *Sibson*, 1982; *Strehlau*, 1986]. In this model, earthquake nucleation and stress drop peak close to the bottom of the brittle unstable domain. In the quartzofeldspathic crust, the brittle-ductile transition is bounded by isotherms corresponding to the onset of ductile behavior in quartz and feldspar occurring at about 300 and 450°C, respectively [*Tullis and Yund*, 1977; *White*, 1975].

A number of authors [e.g., *Burov*, 2010; *Chen et al.*, 2012; *Deverchere et al.*, 2001] have questioned a direct comparison between the brittle-ductile transition and the long-term properties of the crust extrapolated from rock laboratory experiments with temperature, spatial scale, and strain rates orders of magnitude different from those in nature [e.g., *Burov*, 2010; *Chen et al.*, 2012; *Deverchere et al.*, 2001]. Moreover, few studies have examined what effect the assumed strain rate has on computed brittle-ductile transition depths and the implied strength of the crust as a whole [cf. *Zoback and Townend*, 2001; *Zoback et al.*, 2002]. Thus, it can be difficult to draw conclusions regarding bulk rheology from an earthquake depth distribution alone [*Deverchere et al.*, 2001] especially when the period of seismological observation is substantially shorter than a seismic cycle [e.g., *Burov*, 2010; *Chen et al.*, 2012; *Deverchere et al.*, 2001]. As a corollary, while the presence of seismicity does indicate that the crust is sufficiently weak with respect to the ambient stresses to deform brittly, the absence of seismicity within the observation period may mean one of several things: among other explanations, either the strain rates were too low to produce discernible seismicity, irrespective of the prevailing stresses, or the failure criterion has not been met.

4.2. Lateral and Vertical Variations in Seismicity

Our tomographic results and relocated seismicity data set enable us to examine how lateral and vertical variations in seismicity observed adjacent to the Alpine Fault relate to structural features inferred from tomography, which may relate to rock properties and rheology, and to variations in thermal structure, strain rate, and fluid pressure documented in previous studies.

4.2.1. Seismicity Immediately West of the Alpine Fault Trace

The earthquakes at 4–11 km depth within a kilometer of the Alpine Fault (Figure 10) indicate local deepening of the seismic-aseismic transition, probably associated with the transition into the relatively cool footwall [*Townend*, 1999]. Our estimates of the depth of the seismic-aseismic transition and that in the Alpine Fault hanging wall suggest that a large to great Alpine Fault earthquake could reach a depth of 7–11 km in our region of study, although strain rate-dependent shift of brittle behavior into the ductile domain could enable the rupture to propagate a few kilometers deeper [e.g., *Hobbs*, 1986; *Rolandone et al.*, 2004]. In

comparison, on a time scale of 10 years, dislocation modeling of geodetic vertical rates [*Beavan et al.*, 2010] across the central Alpine Fault suggests that coupling on the Alpine Fault diminishes below 7–13 km depth.

4.2.2. Sparse Hanging-Wall Seismicity Within 9 km of the Alpine Fault Trace

Within the bounds of the ALFA09 array we observe a ∼9 km wide strip with low levels of seismicity, immediately southeast of the Alpine Fault trace between X = 0 and X = 9 km (Figures 10 and 13), precluding a reliable estimate of the depth of the seismic-aseismic transition. Few of the earthquake hypocenters in this strip have depths exceeding 7 km, suggesting that the depth to the seismic-aseismic transition (and into the semibrittle domain) is not significantly different from the region further to the southeast.

The high geothermal gradient in the vicinity of the Alpine Fault [*Sutherland et al.*, 2012] and the inferred presence of a fluid phase in the midcrust suggested by low Vp and Vs values (Figures 6 and 7), consistent with observations made in previous geophysical and geological studies [*Craw*, 1997; *Eberhart-Phillips et al.*, 2008; *Holm et al.*, 1989; *Stern et al.*, 2001; *Sutherland et al.*, 2012; *Vry et al.*, 2010; *Wannamaker et al.*, 2002], are likely factors contributing to the shallow seismic-aseismic transition.

A similar interpretation was made by *Boese et al.* [2012] for the region southwest of our study area, where the zone of low seismicity has similar width but surface elevations are higher (Figure 13). This region is associated with the lowest thermochronometric ages near the fault and hence, with maximum uplift and exhumation rates [e.g., *Little et al.*, 2005]. Between the two studies, Harihari in the north and Franz Josef in the south, the zone of low seismicity widens into the 20–30 km wide low-seismicity triangle [*Boese et al.*, 2012; *Eberhart-Phillips*, 1995; *Leitner et al.*, 2001; *O'Keefe*, 2008]. This coincides with a slightly wider metamorphic textural zone IV relative to the regions north and south (Figure 13). The southern transition into the wider textural zone is thought to result from a northward 15–20° decrease in the steepness of the Alpine Fault [*Little et al.*, 2005].

Overall, the extent of low seismicity along-strike of the Alpine Fault appears to coincide with low thermochronometric ages [e.g., *Batt et al.*, 2000; *Herman et al.*, 2009; *Little et al.*, 2005]. Indeed, thermochronology shows persistently low zircon fission track and K-Ar ages ≤6 Ma and Ar-Ar ages ≤10 Ma close to the Alpine Fault between the Hokitika and Karangarua rivers (KR in Figure 1) [e.g., *Batt et al.*, 2000; *Herman et al.*, 2009; *Little et al.*, 2005], located, respectively, north of this study and south of the region of maximum elevations. Minimum ages are reached along the "low-seismicity triangle" between the Whataroa River and Fox Glacier, where zircon and apatite fission track ages are about ≤∼10 Ma as far as ∼15 and 20–30 km southeast of the Alpine Fault, respectively [e.g., *Batt et al.*, 2000; *Herman et al.*, 2009]. The low apparent ages imply generally comparable depths and rates of exhumation and shallowing of isotherms along the entire Hokitika-Karangarua segment, further suggesting that temperature is likely to be the key factor responsible for the shallow seismic-aseismic transition.

4.2.3. Enhanced Hanging-Wall Seismicity Further Than 9 km From the Alpine Fault Trace

The onset of higher rates of seismicity observed 9–20 km southeast from the Alpine Fault is abrupt and approximately coincides with both a strong lateral gradient in seismic velocities and with an increase in horizontal strain rates. Specifically, a tongue of high Vp and high Vs doming at 3–5 km depth (Figure 7) reveals stiffer material that may be acting to concentrate deformation along its margins. In addition, geodetic measurements reveal a pronounced peak in horizontal strain rates approximately 10 km southeast of the Alpine Fault trace, interpreted to reflect the distribution of present-day slip on the deeper portion of the Alpine Fault [*Beavan and Haines*, 2001; *Beavan et al.*, 1999, 2010; *Ellis et al.*, 2006; *Lamb and Smith*, 2013] and on faults of the Main Divide Fault Zone [*Wallace et al.*, 2006]. This peak appears to coincide with the southeastward onset of seismicity, suggesting that lateral variations in strain rate may be the primary factor controlling the elevated rate of hanging wall seismicity further than 9 km from the fault and that the abruptness of this transition is controlled by structural heterogeneity.

The observed 7 km deep seismic-aseismic transition suggests a shallow onset of ductile behavior in quartz. In the Waitangitaona River valley, next to the Whataroa Valley ∼25 km south of this study, a geothermal gradient of 62.6 ± 2.1°C/km was determined from downhole temperature measurements in the DFDP-1B borehole within 100 m of the Alpine Fault trace at Gaunt Creek [*Sutherland et al.*, 2012], suggesting temperatures of 350°C at 5–6 km depth assuming a linear geothermal gradient. To the southeast of the Alpine Fault trace, thermal models of the Southern Alps predict either a slightly shallower [*Koons*, 1987] or slightly deeper [*Shi et al.*, 1996; *Toy et al.*, 2010] brittle-ductile transition, with temperatures of 350–400 and 200–

250°C doming at 5–6 km depth, with the doming occurring at 9–20 km [*Koons*, 1987] or 5–10 km [*Shi et al.*, 1996] southeast of the Alpine Fault trace, or temperatures of 300–350°C at 5–7 km depth at a 9–20 km distance [*Toy et al.*, 2010]. These estimates, and the predicted doming, suggest that in the region of the observed enhanced seismicity, 9–20 km southeast of the Alpine Fault, temperature is likely to be a primary factor contributing to the shallow, ~7 km deep, seismic-aseismic transition.

The elevated rate of seismicity suggests that pervasive brittle fracturing in this region enhances permeability and thus limits pore pressures to hydrostatic levels [cf. *Townend and Zoback*, 2000]. In the midcrust, in contrast, low P wave speeds [*Scherwath et al.*, 2003; *Stern et al.*, 2001], high attenuation [*Eberhart-Phillips et al.*, 2008], and high electrical conductivity [*Wannamaker et al.*, 2002] have been interpreted as indicative of high pore fluid pressures. The transition to a high pore fluid pressure in the midcrust is likely to further contribute to a shallow seismic-aseismic transition. Conversely, closer to the Alpine Fault, the relative lack of seismicity may be insufficient to maintain permeability and relieve fluid overpressures, thereby contributing to lower effective normal stresses, a lower yield strength and consequently, a slightly deeper seismic-aseismic transition within the low-seismicity region compared to that of enhanced seismicity.

To summarize, we interpret the lateral variations in hanging wall seismicity rates, and particularly the abrupt onset of seismicity 9 km from the Alpine Fault trace, to be governed by horizontal strain rate gradients, superimposed upon heterogeneous rheological structure; we interpret the lateral variations in seismicity cutoff depths to reflect different thermal regimes. Seismicity depths may also be controlled by lateral variations in permeability that are themselves related to the variations in rates of seismicity and fracturing.

5. Conclusions

Understanding how intrinsic properties of the fault zone such as lithology and structure interact with extrinsic, possibly time-varying factors such as strain rate, temperature, and fluid pressure is crucial for understanding seismogenesis in active plate boundaries. We have used a combination of seismic tomography, waveform-correlation earthquake relocation, and focal mechanism analysis to characterize in detail the structure of the midcrust adjacent to a section of the central Alpine Fault, which is late in its typical cycle of large (M8) earthquakes.

More than 1300 earthquakes were detected between Harihari and Ross within ~50 km of the central Alpine Fault trace using two temporary seismic arrays deployed consecutively between 2008 and 2010. The dense station spacing of the ALFA seismic arrays yielded well resolved earthquake locations with hypocenter depth errors smaller than 0.6 km.

Distinct variations in the rate of seismicity are observed with distance from the Alpine Fault trace: (1) limited seismicity in the Alpine Fault footwall occurring at 4–11 km depths within 2 km west of the fault trace and exhibiting reverse focal mechanisms ($M_L \leq 3.1$); (2) a 9 km wide strip southeast of the Alpine Fault containing sparse seismicity at depths of 3–8 km; (3) enhanced seismicity in the region between 9 and 20 km southeast of the Alpine Fault, with a seismic-aseismic transition at 7 km depth.

The step in the seismic-aseismic transition across the Alpine Fault is associated with an increase in geothermal gradient from the footwall into the hanging wall. We thus conclude that temperature is the primary factor contributing to the shallow seismic-aseismic transition and to lateral variations in this transition depth. Elevated pore pressures in the midcrust inferred from previous studies also likely contribute to the shallow seismic-aseismic transition southeast of the Alpine Fault, and a feedback process may exist between rates of earthquake-related fracturing, bulk permeability, and ambient fluid pressures. Within the low-seismicity region, the presence of a fluid phase is suggested by low Vp and Vs values at 5–10 km depth that are 8 and 6% lower than to the southeast.

Clusters of earthquakes in the region of enhanced seismicity suggest present-day seismic activity on the deep extensions of faults outcropping in the Southern Alps, or on subparallel structures at depth, which are thought to accommodate some of the remainder (10–15%) of the relative plate motion not accommodated by coseismic slip on the Alpine Fault. To the southeast of this region, the seismicity cutoff depth deepens beneath the foothills where large M6+ earthquakes such as 1994 Arthur's Pass earthquake [*Robinson and McGinty*, 2000] occur. The region of enhanced seismicity is associated with doming of Vp and Vs contours to 3–5 km depth that may represent uplifted material perhaps locally causing higher levels of differential

BOURGUIGNON ET AL.   1039

stress. The onset of enhanced seismicity ~9 km southeast of the Alpine Fault coincides with a peak in horizontal strain rates interpreted to reflect slip on the deeper Alpine Fault and crustal faults above, suggesting a direct link between the high strain rates and the elevated rate of seismicity. The abruptness of the change in seismicity rates is interpreted to reflect the effects of the strong lateral gradients in seismic velocity within the hanging wall, on which the strain rate variations are superimposed.

References

Adams, C. J. (1981), Uplift rates and thermal structure in the Alpine Fault Zone and Alpine Schists, Southern Alps, New Zealand, *Geol. Soc.*, *181*(9), 211–222.

Allis, R. G., and Y. Shi (1995), New insights to temperature and pressure beneath the central Southern Alps, New Zealand, *N. Z. J. Geol. Geophys.*, *38*, 585–592.

Anderson, H., and T. Webb (1994), New Zealand seismicity: Patterns revealed by the upgraded National Seismograph Network, *N. Z. J. Geol. Geophys.*, *37*, 477–493.

Audet, P., M. G. Bostock, N. I. Christensen, and S. M. Peacock (2009), Seismic evidence for overpressured subducted oceanic crust and megathrust fault sealing, *Nature*, *457*, 76–78.

Bannister, S., C. Thurber, and J. Louie (2006), Detailed fault structure highlighted by finely relocated aftershocks, Arthur's Pass, New Zealand, *Geophys. Res. Lett.*, *33*, L18315, doi:10.1029/2006GL027462.

Barth, N. C., V. G. Toy, R. M. Langridge, and R. J. Norris (2012), Scale dependence of oblique plate-boundary partitioning: New insights from LiDAR, central Alpine Fault, New Zealand, *Lithosphere*, *4*, 435–448.

Batt, G. E., and J. Braun (1999), The tectonic evolution of the Southern Alps, New Zealand: Insights from fully thermally coupled dynamical modelling, *Geophys. J. Int.*, *136*, 403–420.

Batt, G. E., J. Braun, B. P. Kohn, and I. McDougall (2000), Thermochronological analysis of the dynamics of the Southern Alps, New Zealand, *Bull. Geol. Soc. Am.*, *112*, 250–266.

Beavan, J., and J. Haines (2001), Contemporary horizontal velocity and strain rate fields of the Pacific-Australian plate boundary zone through New Zealand, *J. Geophys. Res.*, *106*, 741–770.

Beavan, J., et al. (1999), Crustal deformation during 1994–1998 due to oblique continental collision in the central Southern Alps, New Zealand, and implications for seismic potential of the Alpine fault, *J. Geophys. Res.*, *104*, 25,233–25,255.

Beavan, J., P. Tregoning, M. Bevis, T. Kato, and C. Meertens (2002), Motion and rigidity of the Pacific Plate and implications for plate boundary deformation, *J. Geophys. Res.*, *107*(B10), 2261, doi:10.1029/2001JB000282.

Beavan, J., S. Ellis, and L. Wallace (2007), Kinematic constraints from GPS on oblique convergence of the Pacific and Australian Plates, Central South Island, New Zealand, in *A Continental Plate Boundary: Tectonics at South Island, New Zealand*, edited by D. Okaya, T. Stern, and F. Davey, pp. 75–94, AGU, Washington, D. C.

Beavan, J., P. Denys, M. Denham, B. Hager, T. Herring, and P. Molnar (2010), Distribution of present-day vertical deformation across the Southern Alps, New Zealand, from 10 years of GPS data, *Geophys. Res. Lett.*, *37*, L16305, doi:10.1029/2010GL044165.

Berryman, K. R., U. A. Cochran, K. J. Clark, G. P. Biasi, R. M. Langridge, and P. Villamor (2012), Major earthquakes occur regularly on an isolated plate boundary fault, *Science*, *336*, 1690–1693.

Boese, C. M., J. Townend, E. Smith and T. Stern (2012), Microseismicity and stress in the vicinity of the Alpine Fault, central Southern Alps, New Zealand, *J. Geophys. Res.*, *117*, B02302, doi:10.1029/2011JB008460.

Burov, E. B. (2010), The equivalent elastic thickness (T_e), seismicity and the long-term rheology of continental lithosphere: Time to burn-out "creme brulee?": Insights from large-scale geodynamic modelling, *Tectonophysics*, *484*, 4–26.

Cande, S. C., and J. M. Stock (2004), Pacific-Antarctic-Australia motion and the formation of the Macquarie Plate, *Geophys. J. Int.*, *157*, 399–414.

Chamberlain, C. J., D. R. Shelly, J. Townend and T. A. Stern (2014), Low-frequency earthquakes reveal punctuated slow slip on the deep extent of the Alpine Fault, New Zealand, *Geochem. Geophys. Geosyst.*, *15*, 2984–2999, doi:10.1002/2014GC005436.

Chamberlain, C. P., P. K. Zeitler, A. F. Cooper, and T. Stern (1995), Geochronologic constraints of the uplift and metamorphism along the Alpine Fault, South Island, New Zealand, *N. Z. J. Geol. Geophys.*, *38*, 515–523.

Chen, W.-P., and P. Molnar (1983), Focal depths of intracontinental and intraplate earthquakes and their implications for the thermal and mechanical properties of the lithosphere, *J. Geophys. Res.*, *88*, 4183–4214.

Chen, W.-P., S. H. Hung, T.-L. Tseng, M. Brudzinski, Z. Yang, and R. L. Nowack (2012), Rheology of the continental lithosphere: Progress and new perspectives, *Gondwana Res.*, *21*, 4–18.

Christensen, N. I., and D. Okaya (2007), Compressional and shear wave velocities in South Island, New Zealand rocks and their application to the interpretation of seismological models of the New Zealand crust, in *A Continental Plate Boundary: Tectonics at South Island, New Zealand*, edited by D. Okaya, T. Stern, and F. Davey, pp. 123–155, AGU, Washington, D. C.

Cooper, A. F., and R. J. Norris (1994), Anatomy, structural evolution, and slip rate of a plate-boundary thrust: The Alpine Fault at Gaunt Creek, Westland, New Zealand, *Geol. Soc. Am. Bull.*, *106*, 627–633.

Cox, S., and D. J. A. Barrell (2007), Geology of the Aoraki area, *Geol. Map 15*, p. 71, scale 1:250,000, Inst. of Geol. and Nucl. Sci., Lower Hutt, New Zealand.

Cox, S. C., and R. H. Findlay (1995), The Main Divide fault zone and its role in formation of the Southern Alps, New Zealand, *N. Z. J. Geol. Geophys.*, *38*, 489–499.

Cox, S. C., and R. Sutherland (2007), Regional geological framework of South Island, New Zealand, and its significance for understanding the active plate boundary, in *A Continental Plate Boundary: Tectonics at South Island, New Zealand*, edited by D. Okaya, T. Stern, and F. Davey, p. 369, AGU, Washington, D. C.

Cox, S. C., M. W. Stirling, F. Herman, M. Gerstenberger, and J. Ristau (2012), Potentially active faults in the rapidly eroding landscape adjacent to the Alpine Fault, central Southern Alps, New Zealand, *Tectonics*, *31*, TC2011, doi:10.1029/2011TC003038.

Craw, D. (1997), Fluid inclusion evidence for geothermal structure beneath the Southern Alps, New Zealand, *N. Z. J. Geol. Geophys.*, *40*, 43–52.

Davey, F. J. (2010), Crustal seismic reflection profile across the alpine fault and coastal plain at Whataroa, South Island, *N. Z. J. Geol. Geophys.*, *53*, 359–368.

DeMets, C., R. G. Gordon, D. F. Argus, and S. Stein (1994), Effect of recent revisions to the geomagnetic reversal time scale on estimates of current plate motions, *Geophys. Res. Lett.*, *21*, 2191–2194.

Deverchere, J., C. Petit, N. Gileva, N. Radziminovitch, V. Melnikova, and V. San'kov (2001), Depth distribution of earthquakes in the Baikal rift system and its implications for the rheology of the lithosphere, *Geophys. J. Int.*, *146*, 714–730.

Du, W.-X., C. H. Thurber, and D. Eberhart-Phillips (2004), Earthquake relocation using cross-correlation time delay estimates verified with the bispectrum method, *Bull. Seismol. Soc. Am.*, *94*, 856–866.

Eberhart-Phillips, D. (1995), Examination of seismicity in the central Alpine Fault region, South Island, New Zealand, *N. Z. J. Geol. Geophys.*, *38*, 571–578.

Eberhart-Phillips, D., and S. Bannister (2002), Three-dimensional crustal structure in the Southern Alps region of New Zealand from inversion of local earthquake and active source data, *J. Geophys. Res.*, *107*(B10), 2262, doi:10.1029/2001JB000567.

Eberhart-Phillips, D., and A. J. Michael (1993), Three-dimensional velocity structure, seismicity, and fault structure in the Parkfield region, central California, *J. Geophys. Res.*, *98*, 15,737–715,758.

Eberhart-Phillips, D., and M. Reyners (2012), Imaging the Hikurangi Plate interface region, with improved local-earthquake tomography, *Geophys. J. Int.*, *190*, 1221–1242.

Eberhart-Phillips, D., M. Chadwick, and S. Bannister (2008), Three-dimensional attenuation structure of central and southern South Island, New Zealand, from local earthquakes, *J. Geophys. Res.*, *113*, B05308, doi:10.1029/2007JB005359.

Eberhart-Phillips, D., M. Reyners, S. Bannister, M. Chadwick and S. Ellis (2010), Establishing a versatile 3-D seismic velocity model for New Zealand, *Seismol. Res. Lett.*, *81*, 992–1000.

Ellis, S., J. Beavan, D. *Eberhart*-Phillips and B. Stoeckhert (2006), Simplified models of the Alpine Fault seismic cycle: Stress transfer in the mid-crust, *Geophys. J. Int.*, *166*, 386–402.

Grapes, R., and T. Watanabe (1992), Metamorphism and uplift of Alpine schist in the Franz Josef-Fox Glacier area of the Southern Alps, New Zealand, *J. Metamorph. Geol.*, *10*, 171–180.

Grapes, R. H. (1995), Uplift and exhumation of Alpine Schist, Southern Alps, New Zealand: Thermobarometric constraints, *N. Z. J. Geol. Geophys.*, *38*, 525–533.

Grapes, R. H., T. Watanabe, and S. Wallis (1994), Mineral composition variation in Alpine Schist, Southern Alps, New Zealand: Implications for recrystallization and exhumation, *Island Arc*, *3*, 163–181.

Haberland, C., Rietbrock, A., Lange, D., Bataille, K., and Dahm, T. (2009), Structure of the seismogenic zone of the southcentral Chilean margin revealed by local earthquake traveltime tomography, *J. Geophys. Res.*, *114*, B01317, doi:10.1029/2008JB005802.

Hardebeck, J. L., and P. M. Shearer (2002), A new method for determining first-motion focal mechanisms, *Bull. Seismol. Soc. Am.*, *92*, 2264–2276.

Hawkes, M. R. (1991), The effect of bedrock geology on sediment yield in an alpine area of extreme rainfall, MS thesis, Univ. of Canterbury, Christchurch, New Zealand.

Herman, F., S. C. Cox, and P. J. J. Kamp (2009), Low-temperature thermochronology and thermokinematic modeling of deformation, exhumation and development of topography in the central Southern Alps, New Zealand, *Geol. Soc. N. Z. Misc. Publ.*, *128A*, 84–84.

Hobbs, B. E., A. Ord, and C. Teyssier (1986), Earthquakes in the ductile regime?, *Pure Appl. Geophys.*, *124*, 309–336.

Holm, D. K., R. J. Norris, and D. Craw (1989), Brittle and ductile deformation in a zone of rapid uplift: Central Southern Alps, New Zealand, *Tectonics*, *8*, 153–168.

Jenkin, G. R. T., D. Craw and A. E. Fallick, (1994), Stable isotopic and fluid inclusion evidence for meteoric fluid penetration into an active mountain belt: Alpine Schist, New Zealand, *J. Metamorph. Geol.*, *12*, 429–444.

Kissling, E. (1988), Geotomography with local earthquake data, *Rev. Geophys.*, *26*, 659–698.

Koons, P. O. (1987), Some thermal and mechanical consequences of rapid uplift: An example from the Southern Alps, New Zealand, *Earth Planet. Sci. Lett.*, *86*, 307–319.

Koons, P. O. (1989), The topographic evolution of collisional mountain belts: A numerical look at the Southern Alps, New Zealand, *Am. J. Sci.*, *289*, 1041–1069.

Koons, P. O. (1995), Modeling the topographic evolution of collisional belts, *Annu. Rev. Earth Planet. Sci.*, *23*, 375–408.

Lamb, S., and E. Smith (2013), The nature of the plate interface and driving force of interseismic deformation in the New Zealand plate-boundary zone, revealed by the continuous GPS velocity field, *J. Geophys. Res. Solid Earth*, *118*, 3160–3189, doi:10.1002/jgrb.50221.

Langridge, R. M., P. Villamor, R. Basili, P. Almond, J. J. Martinez-Diaz, and C. Canora (2010), Revised slip rates for the Alpine fault at Inchbonnie: Implications for plate boundary kinematics of South Island, New Zealand, *Lithosphere*, *2*, 139–152.

Leitner, B., D. *Eberhart*-Phillips, H. Anderson and J. L. Nabelek (2001), A focused look at the Alpine fault, New Zealand: Seismicity, focal mechanisms, and stress observations, *J. Geophys. Res.*, *106*, 2193–2220.

Little, T. A., R. J. Holcombe, and B. R. Ilg (2002), Kinematics of oblique collision and ramping inferred from microstructures and strain in middle crustal rocks, Central Southern Alps, New Zealand, *J. Struct. Geol.*, *24*, 219–239.

Little, T. A., S. Cox, J. K. Vry, and G. Batt (2005), Variations in exhumation level and uplift rate along the oblique-slip Alpine fault, central Southern Alps, New Zealand, *Bull. Geol. Soc. Am.*, *117*, 707–723.

Little, T. A., V. G. Toy, D. J. Prior, B. G. Gillam, S. Kidder, A. Cross, S. Ellis, and O. Al'bot, (2013), Foliation fanning in the hangingwall of the Alpine Fault, central Southern Alps, in *Geosciences 2013 Conference*, edited by C. M. Reid and A. Wandres, p. 107, Geosci. Soc. of N. Z., Christchurch, New Zealand.

Meissner, R., and J. Strehlau (1982), Limits of stresses in continental crusts and their relation to the depth-frequency distribution of shallow earthquakes, *Tectonics*, *1*, 73–89.

Mortimer, N. (2004), New Zealand's geological foundations, *Gondwana Res.*, *7*, 261–272.

Nikias, C., and M. R. Raghuveer (1987), Bispectrum estimation: A digital signal processing framework, *Proc. IEEE*, *75*, 869–891.

Nikias, C. L., and R. Pan (1988), Time delay estimation in unknown Gaussian spatially correlated noise, *IEEE Trans. Acoust. Speech Signal Process.*, *36*, 1706–1714.

Norris, R. J., and A. F. Cooper (1997), Erosional control on the structural evolution of a transpressional thrust complex on the Alpine Fault, New Zealand, *J. Struct. Geol.*, *19*, 1323–1342.

Norris, R. J., and A. F. Cooper (2001), Late Quaternary slip rates and slip partitioning on the Alpine Fault, New Zealand, *J. Struct. Geol.*, *23*, 507–520.

Norris, R. J., and A. F. Cooper (2003), Very high strains recorded in mylonites along the Alpine Fault, New Zealand: Implications for the deep structure of plate boundary faults, *J. Struct. Geol.*, *25*, 2141–2157.

Norris, R. J., and A. F. Cooper (2007), The Alpine Fault, New Zealand: Surface geology and field relationships, in *A Continental Plate Boundary: Tectonics at South Island, New Zealand, Geophys. Monogr.*, *175*, edited by D. Okaya, T. Stern and F. Davey, pp. 157–175, AGU, Washington, D. C.

O'Connell, R. J., and B. Budiansky (1974), Seismic velocities in dry and saturated cracked solids, *J. Geophys. Res.*, *79*, 5412–5426.

Okaya, D., N. Christensen, D. Stanley, and T. Stern (1995), Crustal anisotropy in the vicinity of the Alpine Fault Zone, South Island, New Zealand, *N. Z. J. Geol. Geophys.*, *38*, 579–583.

Okaya, D., T. Stern, F. Davey, S. Henrys and S. Cox (2007), Continent-continent collision at the Pacific/Indo-Australian plate boundary: Background, motivation, and principal results, in *A Continental Plate Boundary: Tectonics at South Island, New Zealand*, edited by D. Okaya, T. Stern, and F. Davey, pp. 1–18, AGU, Washington, D. C.

O'Keefe, B. C. (2008), Microseismicity of the Central Alpine Fault region, New Zealand, MS thesis, Vic. Univ. of Wellington, Wellington, New Zealand.

Reasenberg, P., and D. Oppenheimer (1985), FPFIT, FPPLOT, and FPPAGE: FORTRAN computer programs for calculating and displaying earthquake fault-plane solutions, *U.S. Geol. Surv. Open File Rep.*, *85–739*, p. 109.

Reed, J. J. (1964), Mylonites, cataclasites, and associated rocks along the Alpine fault, South Island, New Zealand, *N. Z. J. Geol. Geophys.*, *7*, 645–684.

Reyners, M. (1988), Reservoir-induced seismicity at Lake Pukaki, New Zealand, *Geophys. J. R. Astron. Soc.*, *93*, 127–135.

Ristau, J. (2008), Implementation of routine regional moment tensor analysis in New Zealand, *Seismol. Res. Lett.*, *79*, 400–415.

Robinson, R., and P. J. McGinty (2000), The enigma of the Arthur's Pass, New Zealand, earthquake: 2. The aftershock distribution and its relation to regional and induced stress fields, *J. Geophys. Res.*, *105*, 16,139–16,150.

Rolandone, F., R. Burgmann, and R. M. Nadeau (2004), The evolution of the seismic-aseismic transition during the earthquake cycle: Constraints from the time-dependent depth distribution of aftershocks, *Geophys. Res. Lett.*, *31*, L23610, doi:10.1029/2004GL021379.

Scales, J. A. (1989), On the use of conjugate gradient to calculate the eigenvalues and singular values of large, sparse matrices, *Geophys. J. R. Astron. Soc.*, *97*, 179–183.

Scherwath, M., T. Stern, F. Davey, D. Okaya, W. S. Holbrook, R. Davies, and S. Kleffmann (2003), Lithospheric structure across oblique continental collision in New Zealand from wide-angle P wave modeling, *J. Geophys. Res.*, *108*(B12), 2566, doi:10.1029/2002JB002286.

Scholz, C. H. (1988), The brittle-plastic transition and the depth of seismic faulting, *Geol. Rundsch.*, *77*, 319–328.

Shi, Y., R. Allis, and F. Davey (1996), Thermal modeling of the southern alps, New Zealand, *Pure Appl. Geophys.*, *146*, 469–501.

Sibson, R. H. (1982), Controls on the depth and style of seismic activity in continental crust, *Earthquake Notes*, *54*, 63–63.

Sibson, R. H., S. H. White, and B. K. Atkinson (1979), Fault rock distribution and structure within the Alpine fault zone: A preliminary account, *Bull. R. Soc. N. Z.*, *18*, 55–65.

Simon, N., M. S. Rattenbury, and R. P. Suggate (2002), Geology of the Greymouth area, *Geol. Map 12*, scale 1:250,000, Inst. of Geol. Nucl. Sci., Lower Hutt, New Zealand.

Stern, T., S. Kleffmann, D. Okaya, M. Scherwath, and S. Bannister (2001), Low seismic-wave speeds and enhanced fluid pressure beneath the Southern Alps of New Zealand, *Geology*, *29*, 679–682.

Stern, T., D. A. Okaya, S. Kleffmann, M. Scherwath, S. Henrys, and F. J. Davey (2007), Geophysical exploration and dynamics of the Alpine fault zone, in *A Continental Plate Boundary: Tectonics at South Island, New Zealand, Geophys. Monogr.*, *175*, edited by D. Okaya, T. Stern and F. Davey, pp. 207–233, AGU, Washington, D. C.

Strehlau, J. (1986), A discussion of the depth extent of rupture in large continental earthquakes, in *Earthquake Source Mechanics*, edited by S. Das, J. Boatwright, and C. H. Scholz, pp. 131–145, AGU, Washington, D. C.

Sutherland, R. (1999), Cenozoic bending of New Zealand basement terranes and Alpine Fault displacement: A brief review, *N. Z. J. Geol. Geophys.*, *42*, 295–301.

Sutherland, R., K. Berryman, and R. Norris (2006), Quaternary slip rate and geomorphology of the Alpine Fault: Implications for kinematics and seismic hazard in southwest New Zealand, *Geol. Soc. Am. Bull.*, *118*, 464–474.

Sutherland, R., et al. (2007), Do great earthquakes occur on the Alpine Fault in Central South Island, New Zealand?, in *A Continental Plate Boundary: Tectonics at South Island, New Zealand*, edited by D. Okaya, T. Stern, and F. Davey, p. 369, AGU, Washington, D. C.

Sutherland, R., et al. (2012), Drilling reveals fluid control on architecture and rupture of the Alpine Fault, New Zealand, *Geology*, *40*, 1143–1146.

Takei, Y. (2002), Effect of pore geometry on VP/VS: From equilibrium geometry to crack, *J. Geophys. Res.*, *107*(B2), 2043, doi:10.1029/2001JB000522.

Tippett, J. M., and P. J. J. Kamp (1993), Fission track analysis of the late Cenozoic vertical kinematics of continental Pacific crust, South Island, New Zealand, *J. Geophys. Res.*, *98*, 16,119–16,148.

Toomey, D. R., and G. R. Foulger (1989), Tomographic inversion of local earthquake data from the Hengill-Grensdalur central volcano complex, Iceland, *J. Geophys. Res.*, *94*, 17,497–17,510.

Townend, J. (1999), Heat flow through the West Coast, South Island, New Zealand, *N. Z. J. Geol. Geophys.*, *42*, 21–31.

Townend, J., and M. D. Zoback (2000), How faulting keeps the crust strong, *Geology*, *28*, 399–402.

Townend, J., R. Sutherland, and V. Toy (2009), Deep fault drilling project-Alpine Fault, New Zealand, *Sci. Drill.*, *8*, 75–82.

Townend, J., S. Sherburn, R. Arnold, C. Boese, and L. Woods (2012), Three-dimensional variations in present-day tectonic stress along the Australia–Pacific plate boundary in New Zealand, *Earth Planet. Sci. Lett.*, *353–354*, 47–59.

Townend, J., R. Sutherland, V. G. Toy, J. D. Eccles, C. Boulton, S. C. Cox, and D. McNamara (2013), Late-interseismic state of a continental plate-bounding fault: Petrophysical results from DFDP-1 wireline logging and core analysis, Alpine Fault, New Zealand, *Geochem. Geophys. Geosyst.*, *14*, 3801–3820, doi:10.1002/ggge.20236.

Toy, V. G., D. Craw, A. F. Cooper, and R. J. Norris (2010), Thermal regime in the central Alpine Fault zone, New Zealand: Constraints from microstructures, biotite chemistry and fluid inclusion data, *Tectonophysics*, *485*, 178–192.

Toy, V. G., R. J. Norris, D. J. Prior, M. Walrond, and A. F. Cooper (2013), How do lineations reflect the strain history of transpressive shear zones? The example of the active Alpine Fault zone, New Zealand, *J. Struct. Geol.*, *50*, 187–198.

Tullis, J., and R. A. Yund (1977), Experimental deformation of dry westerly granite, *J. Geophys. Res.*, *82*, 5705–5718.

Turnbull, I. M., N. Mortimer, and D. Craw (2001), Textural zones in the Haast Schist: A reappraisal, *N. Z. J. Geol. Geophys.*, *44*, 171–183.

Van Avendonk, H. J. A., W. S. Holbrook, D. Okaya, J. K. Austin, F. Davey, and T. Stern (2004), Continental crust under compression: A seismic refraction study of South Island Geophysical Transect I, South Island, New Zealand, *J. Geophys. Res.*, *109*, B06302, doi:10.1029/2003JB002790.

Vry, J., R. Powell, K. M. Golden, and K. Petersen (2010), The role of exhumation in metamorphic dehydration and fluid production, *Nat. Geosci.*, *3*, 31–35.

Waight, T. E., S. D. Weaver, T. R. Ireland, R. Maas, R. J. Muir, and D. Shelley (1997), Field characteristics, petrography, and geochronology of the Hohonu Batholith and the adjacent Granite Hill Complex, North Westland, New Zealand, *N. Z. J. Geol. Geophys.*, *40*, 1–17.

Walcott, R. I. (1998), Modes of oblique compression: Late Cenozoic tectonics of the South Island of New Zealand, *Rev. Geophys.*, *36*, 1–26.

Waldhauser, F. (2001), HypoDD: A computer program to compute double-difference hypocenter locations, *U.S. Geol. Surv. Open File Rep.*, 01–113, p. 25.

Wallace, L. M., J. Beavan, R. McCaffrey, K. Berryman, and P. Denys (2006), Balancing the plate motion budget in the South Island, New Zealand using GPS, geological and seismological data, *Geophys. J. Int.*, *168*, 332–352.

Wannamaker, P. E., G. R. Jiracek, J. A. Stodt, T. G. Caldwell, V. M. Gonzalez, J. D. McKnight, and A. D. Porter (2002), Fluid generation and pathways beneath an active compressional orogen, the New Zealand Southern Alps, inferred from magnetotelluric data, *J. Geophys. Res.*, *107*(B6), 2117, doi:10.1029/2001JB000186.

Wech, A. G., C. M. Boese, T. A. Stern, and J. Townend (2012), Tectonic tremor and deep slow slip on the Alpine Fault, *Geophys. Res. Lett.*, *39*, L10303, doi:10.1029/2012GL051751.

Wech, A. G., A. F. Sheehan, C. M. Boese, J. Townend, T. A. Stern, and J. A. Collins (2013), Tectonic tremor recorded by ocean bottom seismometers, *Seismol. Res. Lett.*, *84*, 752–758.

Wellman, H. W. (1979), An uplift map for the South Island of New Zealand, and a model for uplift of the Southern Alps, *Bull. R. Soc. N. Z.*, *18*, 13–20.

Wessel, P., and W. H. F. Smith (1991), Free software helps map and display data, *Eos Trans. AGU*, *72*, 441–446.

White, S. (1975), Tectonic deformation and recrystallisation of oligoclase, *Contrib. Mineral. Petrol.*, *50*, 287–304.

Willett, S. D., and M. T. Brandon (2002), On steady states in mountain belts, *Geology*, *30*, 175–178.

Zhang, H., and C. H. Thurber (2003), Double-difference tomography: The method and its application to the Hayward Fault, California, *Bull. Seismol. Soc. Am.*, *93*, 1875–1889.

Zhang, H., C. Thurber, and P. Bedrosian (2009), Joint inversion for Vp, Vs, and Vp/Vs at SAFOD, Parkfield, California, *Geochem. Geophys. Geosyst.*, *10*, Q11002, doi:10.1029/2009GC002709.

Zoback, M. D., and J. Townend (2001), Implications of hydrostatic pore pressures and high crustal strength for the deformation of intraplate lithosphere, *Tectonophysics*, *336*, 19–30.

Zoback, M. D., J. Townend, and B. Grollimund (2002), Steady-state failure equilibrium and deformation of intraplate lithosphere, *Int. Geol. Rev.*, *44*, 383–401.